Charged Particle Multiplicities in Electron-Positron Annihilation at Center-of-Mass Energies from 50 to 61.4 GeV

by
Hong Wei Zheng

Submitted in Partial Fulfillment
of the
Requirements for the Degree

DOCTOR OF PHILOSOPHY

Supervised by Professor S.L. Olsen

Department of Physics and Astronomy
University of Rochester
Rochester, New York

June 1990

Abstract

We present the charged particle multiplicity distributions for e^+e^- annihilation at center-of-mass energies from 50 to 61.4 GeV. The results are based on a data sample corresponding to a total integrated luminosity of 29.6 pb^{-1} obtained with the AMY detector at the TRISTAN storage ring. The charged particle multiplicity distributions deviate significantly from the modified-Poisson and pair-Poisson distributions, but follow KNO scaling and are well reproduced by the Lund parton-shower model.

VITA

The author was born in Henan Province, China in 1956. He spent his undergraduate and graduate studies at the Modern Physics Department of the University of Science and Technology of China (USTC). During the two and half years of his graduate studies, he was engaged in an experiment measuring the electron-neutrino mass by using the USTC iron-free double focusing β-spectrometer. His thesis adviser was Prof. J. Y. Mei. He received an M.S.(Physics) in Jan. 1983 from USTC. After that he joined the Institute for High Energy Physics (IHEP) of the Chinese Academy of Science and participated in the construction of a general detector for Beijing Electron Positron Collider. He has been a research assistant in high energy physics since then. He has been engaged in the AMY experiment at the TRISTAN accelerator at KEK , Japan, from its design and construction stages. He became a graduate student of the Department of Physics and Astronomy of the University of Rochester in Jan. 1986. He received an M.A. from Rochester in Feb. 1989. His thesis adviser has been Prof. S.L. Olsen.

Acknowledgements

My thesis would not have been possible, except for the excellent and diligent work of many people: the CDC sub-group, all the collaborators in the AMY experiment, and the TRISTAN and KEK staffs.

I would like to express my deepest thank to Stephen L. Olsen for his continuous encouragment and advise during my graduate study at University of Rochester as well as his friendship and kindly support over the years. I have gained much invaluable knowledge of many things from my association with him.

In particular, I would like to thank Patrice Perez, the analysis presented in this thesis had been carried out under his guidance. In addition, I am grateful for the time and effort Alan Sill took in helping to run the Monte Carlo simulation and analysis in VAX. I am deeply indebted to Arie Bodek for his enthusiasm to answer questions and for his valuable help and support; to Ed Thorndike for many useful suggestions and comments about the multiplicity analysis; to Aki Maki and Kazou Abe for their support during my stay at KEK.

I can never forget that Satoshi Ozaki, Ming-Han Ye and Chi-Peng Cheng are responsible for providing me the important chance to join AMY experiment.

It is my pleasure to thank Rosemarie Olsen; her friendship and warmth has helped to make my wife and I feel as though we were part of her family.

Finally, I would like to thank my Mother, Father and the rest of my family; they have always encouraged me to set ambitious goals, and helped me to obtain them.

This thesis is dedicated to my wife, Lu, our parents, and our children Lucy and Amy, for their love and understanding through these trying times.

Contents

1 Introduction 1

1.1 Hadron Production 1

1.2 Charged Hadron Multiplicity 3

1.2.1 Average Value of The Charged Multiplicity 3

1.2.2 Charged Multiplicity Distribution 6

1.3 Scope of this Thesis 9

2 TRISTAN and The AMY Experiment 11

2.1 TRISTAN 11

2.2 AMY 13

2.2.1 The Inner Tracking Chamber 16

2.2.2 Central Drift Chamber 16

2.2.3 Barrel Electromagnetic Calorimeter 19

2.2.4 The Superconducting Magnet 21

2.2.5 Muon Chamber 22

2.2.6 The Endcap Detector 23

2.2.7 The X-Ray Detector and the Trigger Counters 24

2.2.8 Trigger Systems and Data Acquisition 24

2.3 Monte Carlo Simulation 25

2.3.1 Hadronic Event Generation 27

2.3.2 Detector Simulation 30

2.4 Charged Particle Track Reconstruction 34

2.4.1 Tracking Program 34

2.4.2 Track Reconstruction Efficiency 35

2.5 Hadronic Event Selection 37

2.5.1 Charged Track Selection 37

2.5.2 Hadronic Event Selection 41

3 Determination of the Charged Hadron Multiplicity 44

3.1 Observed Multiplicity Distribution 44

3.2 Corrections 44

3.2.1 Origin of the Correction 44

3.2.2 Correction for Detector Effects 46

3.2.3 Correction for Initial State Radiation 49

3.3 Systematic Errors 50

3.3.1 Selection Efficiency 50

3.3.2 CDC Smearing 50

3.3.3 Initial-state Radiation 50

3.3.4 $\gamma \rightarrow e^+e^-$ Conversion 53

3.3.5 MC Event Generator 56

3.3.6 Low Multiplicity 56

3.3.7 Event Selection Cut 58

3.4 Point-to-point Systematic Error 58

4 Results 60

4.1 Charged Multiplicity Distribution 60

4.2 Energy Dependence of The Charged Multiplicity 67

4.3 KNO Scaling 69

5 Conclusion 75

A The Central Drift Chamber of the AMY Detector 76

B List of the AMY Collaborators 84

List of Tables

2.1 SHC resolution, in form $\sigma_E/E = a \times E^{-1/2} + b$, SHC analysis version 522. 21

2.2 SHC resolution sextant-by-sextant, for Bhabha events, SHC analysis version 522. 22

2.3 CDC smeared resolution parameters. 33

2.4 AMY luminosities for given center-of-mass energies. Errors are statistical only. 38

3.1 Summary of the systematic error of $< n >$. 58

4.1 The charged multiplicity distributions $1/N_{ev}$ (dN/dn) in percent. The final column lists the results from all energies combined (average center-of-mass energy equals to 57 GeV). Statistical errors are listed first and systematic errors second. For the $n = 2$ and $n = 4$ points only systematic errors are given. 62

4.2 Summaries of the multiplicity distributions at each energy. 65

A.1 The drift chamber configuration 81

A.2 Properties of materials used in the CDC. 83

List of Figures

1.1 Feynman diagram for e^+e^- annihilation into a quark-antiquark pair. 2

1.2 A typical 2-jet hadronic event recorded by the AMY detector. . . . 4

1.3 The average charged multiplicity in e^+e^- annihilation as a function of center-of-mass energy. This figure includes data available prior to the experiment reported here. The curves show the fits to the data (see text). 5

1.4 The corrected charged multiplicity distribution for HRS experiment compared with the modified-Poisson (dash curve), and pair-Poisson (solid curve) distributions. 7

1.5 The corrected charged multiplicity distribution for the TASSO experiment compared with the modified-Poisson (dash curve), and pair-Poisson (solid curve) distributions. 8

2.1 The TRISTAN e^+e^- Collider 12

2.2 The AMY Detector 15

2.3 The Central Drift Chamber (CDC) of the AMY detector. 17

2.4 The Shower Counter (SHC) 20

2.5 AMY's data aquisition system 26

2.6 The momentum distributions of charged particles (a) and of neutral particles (b) for the real data (points) and the data generated by Lund 6.3. (histogram) for 56 GeV. 31

2.7 The CDC time residual distribution for experiment data (points) and MC simulation (histogram). 33

2.8 Distribution of R_{mix}^{obs} for the data and simulated MC events. The solid line (dashed line) indicates the Parton-Shower (Matrix-Element) model. 36
2.9 The track-reconstruction efficiency as a function of R_{mix}. 38
2.10 The track-reconstruction efficiency as a function of the transverse momentum. 39
2.11 The track-reconstruction efficiency as a function of θ, the polar angle with respect to the e^+e^- beam direction. 40

3.1 The observed charged hadron multiplicity distribution at center-of-mass energy equals to 56 GeV compared with simulated events generated with (a) the Lund 6.3 and (b) the Lund 6.2 Monte Carlo event generators. 45
3.2 The observed multiplicity distributions for generated multiplicities of $n = 8$ a), 14 b), 20 c), and 24 d), as determined from the 56 GeV Monte Carlo simulated data sample. 47
3.3 The enclosed area indicates the r.m.s. range in values of the observed charged multiplicity m for different values of the generated multiplicity n, as determined from simulated Monte Carlo events. The dashed line corresponds to $m = n$. 48
3.4 The charged multiplicity distribution for the total generated events (histogram) and the generated events which failed our acceptance and selection criteria (points). 51
3.5 The CDC time residual distribution for the experimental data (points) and the MC simulated data with a smearing parameter increased by a factor of 1.5. The poor agreement between data and MC in this figure should be compared with the results for our preferred values of the smearing parameters shown in Fig. 2.7. 52
3.6 The energy spectrum of the initial state radiated photon produced by the Lund 6.3 generator. 54

3.7 The integral distribution of the fraction of accepted MC events that contain initial state radiation photons with energies between E_γ and $0.99E_{beam}$. From this we estimate the fraction of events in the data with photon energy between $0.99E_{beam}$ and E_{beam} to be less than 0.05%. 55
3.8 The χ^2 distribution as a function of f 57
3.9 The multiplicity distribution of the experiment data at center-of-mass energy equals to 56GeV corrected by Lund 6.3 (solid points) and Lund 6.2 (open boxes) correction matrix, compare with Lund 6.3 MC (solid histogram) and Lund 6.2 (dotted histogram) 59

4.1 The corrected charged multiplicity distribution for all energies combined compared with the predictions of the Lund 6.3 (Parton-Shower and String-Fragmentation) model (solid histogram), the modified-Poisson (dot-dash curve), and pair-Poisson (dashed curve) distributions. The mean center-of-mass energy is 57 GeV. 61
4.2 The average charged multiplicity in e^+e^- annihilation as a function of center-of-mass energy, including results from other experiments. The curves show the fits to the data (see text). 68
4.3 (a) The energy dependence of the dispersion D. (b) The energy dependence of $< n > /D$. The dashed curve is the expectation for a pair-Poisson behaviour, the solid curve is that for a modified-Poisson. 70
4.4 Fit quality for $< n > /D =$ constant for different values of the lower energy cut-off. 71
4.5 The KNO charged multiplicity distribution for the combined data of this experiment compared with measurements at lower energies and with the fitted Gamma distributions. 73
4.6 The KNO charged multiplicity distribution for the combined data of this experiment compared with measurements at lower energies and with the fitted negative binomial distributions. 74

A.1 The endplate of the AMY central drift chamber. 77
A.2 The wire holding mechanism at the CDC endplate. 78

A.3 A quarter of the CDC endplate. 80

Chapter 1

Introduction

In e^+e^- annihilation, the dynamics of the initial state electron and positron are well described by quantum eletrodynamics. All discrete additive quantum numbers (charge, baryon number, lepton number, strangeness,...) in the initial state sum to zero, and, therefore, all of the initial state energy can be transformed to final states that have the quantum numbers of a photon: spin one, negative parity, and negative charge conjugation. Electron-positron annihilation provides a unique probe for the study of hadronic interactions.

TRISTAN, the electron-positron collider at the National Laboratory for High Energy Physics (KEK), Japan, first had e^+e^- collisions in the winter of 1986, opening up a new high-energy frontier for e^+e^- physics, replacing PETRA [1], the storage ring at the DESY laboratory in Hamburg, West Germany, which terminated operations in 1986. TRISTAN has operated at center-of-mass energy ($\sqrt{s}$) 50 to 61.4 GeV ranges.

The AMY detector, a 3-Tesla superconducting solenoid magnet enclosing tracking and electromagnetic shower detectors, is a general purpose detector with good lepton identification and with high momentum resolution that has been operating at one of the intersecting regions of TRISTAN, called OHO hall.

1.1 Hadron Production

In the TRISTAN energy range, it is expected that e^+e^- annihilation to hadrons takes place via $e^+e^- \rightarrow (\gamma, Z) \rightarrow q\bar{q}$, as shown in Fig. 1.1, with the point-like quarks subsequently fragmenting into hadrons. Occasionally, before hadronizing,

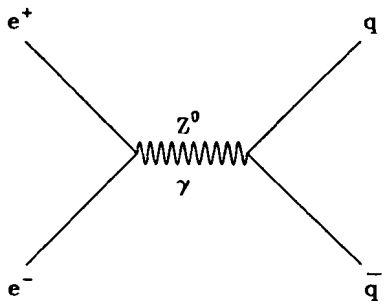

Figure 1.1: Feynman diagram for e^+e^- annihilation into a quark-antiquark pair.

a final state quark will radiate a hard gluon, i.e. $e^+e^- \to (\gamma, Z) \to q\bar{q}g$.

At TRISTAN energies, the quarks produced in $e^+e^- \to q\bar{q}$ have high momentum. They "fragment" into hadrons by a process whose details are not well understood theoretically. This fragmentation, or hadronization, process can be viewed as a repeated sequence of "decays"

$$q \to q' + hadron.$$

This fragmentation process reflects the confinement property of quantum chromodynamics (QCD) which are not amenable to perturbation theory and thus poorly understood. Many of the hadrons produced in the fragmentation process are unstable. These unstable particles decay further with decay chains of varying complexity. The theoretical understanding of these decays is again (with a few exceptions) rather poor. Finally, the end products of the decay chains are observed in detectors, which, in terms of the typical decay length scales, are placed far away. It is from the particles observed here that experimentalists try to study the physics of the initial perturbative stage!

It has been observed that in the hadronization process the longitudinal momentum (with respect to the parton direction) of the hadron grows as the parton

momentum grows , while the momentum component transverse to the parton direction, P_t, of the hadron remains limited ($\sim$ 300MeV/c). Thus, a striking feature of the hadrons coming from a high energy quark is that they collimate within a narrow cone around the original quark direction, thus forming a jet. Fig. 1.2 shows a typical 2-jet hadronic event recorded by the AMY detector.

1.2 Charged Hadron Multiplicity

The charged particle multiplicity, the total number of charged particles produced in an event, in e^+e^- annihilation into multi-hadron final states is one of the most fundamental observables in the fragmentation process. It has been measured whenever a new energy regime has been accessed.

1.2.1 Average Value of The Charged Multiplicity

In the absence of a fundamental theory, a number of phenomenological models, starting with Heisenberg in 1939 [2], have been proposed to characterize the charged multiplicity in high energy hadron processes. In 1950, Fermi used statistical arguments to predict that the average number of charged particles produced in high energy collisions would increase with increasing center-of-mass energy as [3]:

$$< n >= a \cdot s^{1/4}. \tag{1.1}$$

More recent models, motivated by perturbative QCD calculations of the evolution of partons in a leading logarithm approximation, predict

$$< n >= a + b \cdot \exp\left[c\sqrt{\ln(s/Q_0^2)}\right] \tag{1.2}$$

where Q_0 is related to the Λ cutoff parameter of QCD [4, 5, 6] and c is given hy $\sqrt{72/(33-2n_f)} = 1.769$ for $n_f = 5$ [4].

An analysis of pp data suggests the empirical form [7]:

$$< n >= a + b \cdot \ln s + c \cdot \ln^2 s. \tag{1.3}$$

The average charged multiplicity in e^+e^- annihilation as a function of center-of-mass energy is shown in Fig. 1.3.

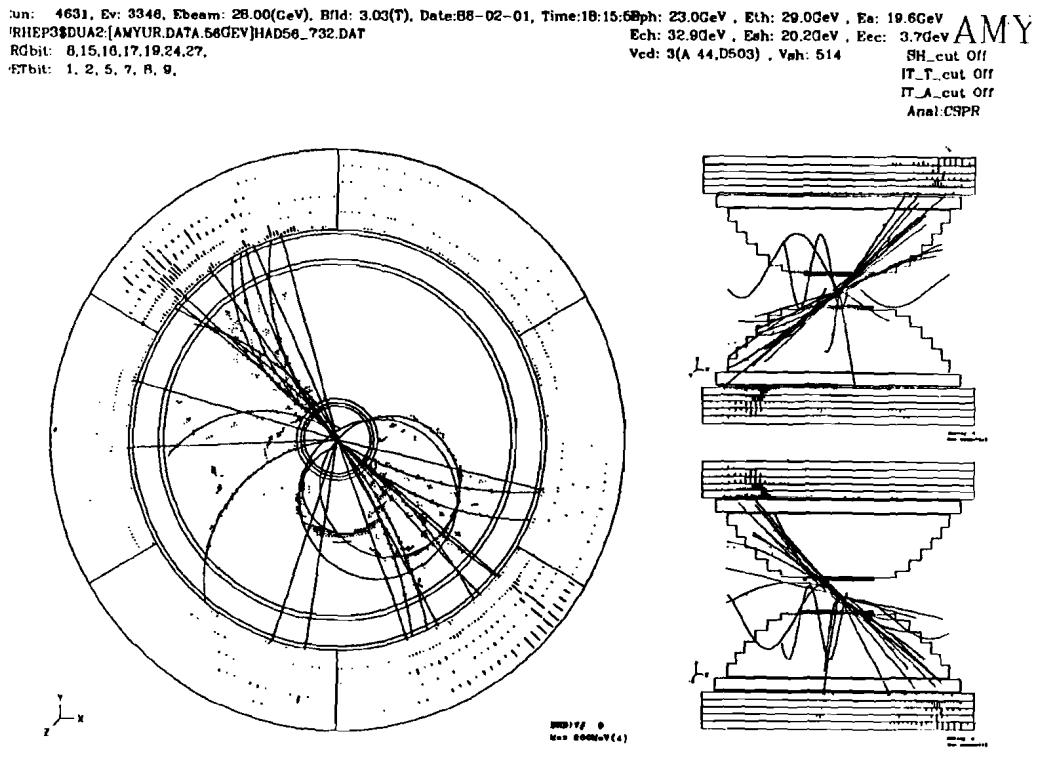

Figure 1.2: A typical 2-jet hadronic event recorded by the AMY detector.

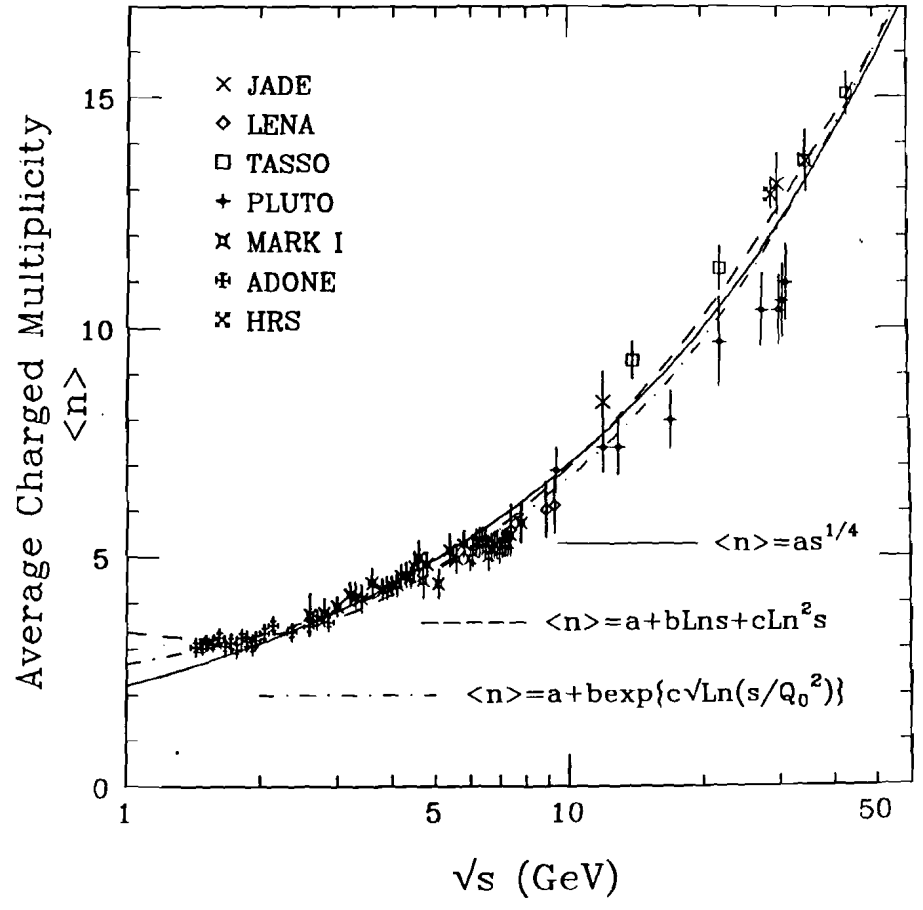

Figure 1.3: The average charged multiplicity in e^+e^- annihilation as a function of center-of-mass energy. This figure includes data available prior to the experiment reported here. The curves show the fits to the data (see text).

1.2.2 Charged Multiplicity Distribution

The relative probability for events of different multiplicities at a given energy, the so-called multiplicity distributions $P(n)$, have generated considerable interest among phenomenologists.

KNO Scaling

In 1972, Koba-Nielson-Olesen (KNO) [8], starting from Feynman scaling [9] and with no further dynamical assumptions, derived the asymptotic result that the product of the mean charged multiplicity $< n >$ and the probability P(n) for n charged particles in the final state is given by a universal function:

$$\psi(\frac{n}{< n >}) = P(n) < n > . \tag{1.4}$$

If the charged multiplicity distribution obeys KNO scaling, then the dispersion D $(=\sqrt{< n^2 > - < n >^2})$ is proportional to $< n >$, i.e. $< n > /D$ is independent of the center-of-mass energy.

KNO scaling appears to be valid in e^+e^- annihilation from 5-45GeV, and over a wide range of energies in pp and $p\bar{p}$ collisions.

Modified- and Pair-Poisson Distribution

Chou and Yang [11] used a different approach and argued that the production of so many particles is indicative of a stochastic process and, thus, should have a Poisson-like behaviour. In this case $D \propto \sqrt{< n >}$, which means that at sufficiently high energies the distribution would be narrower than that expected from KNO scaling.

The comparison of the charged particle multiplicity distribution with Poisson expectations is complicated by the fact that, since electric charge is conserved, charged particles are always produced in pairs. The HRS experiment reported charged multiplicity distributions at $\sqrt{s}$= 29 GeV (Fig. 1.4) which are in excellent agreement with the "modified-Poisson" form [12],

$$\begin{aligned} P^{mod}(n) &= 2\frac{< n >^n e^{-<n>}}{n!} && n = even \\ &= 0 && n = odd. \end{aligned} \tag{1.5}$$

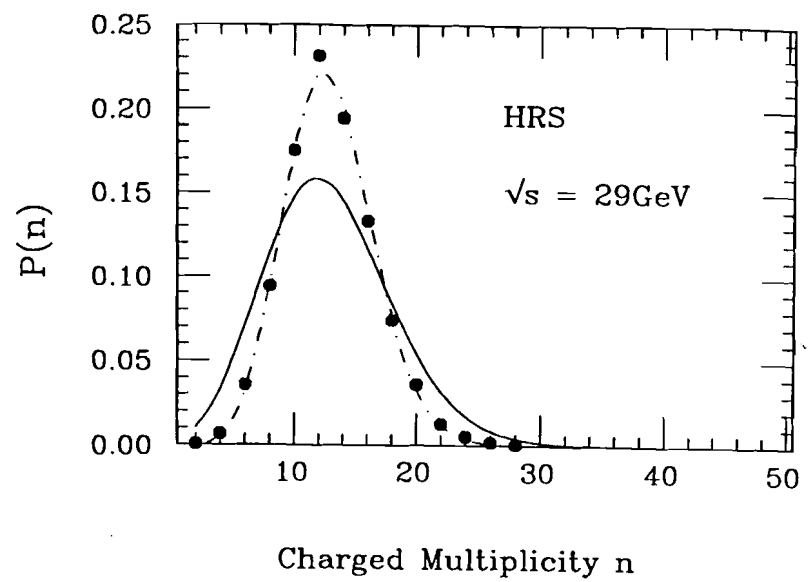

Figure 1.4: The corrected charged multiplicity distribution for HRS experiment compared with the modified-Poisson (dash curve), and pair-Poisson (solid curve) distributions.

A modified Poisson has an r.m.s. width $D = \sqrt{< n >}$. The TASSO experiment has also reported data at $\sqrt{s}$ = 14, 22 GeV (Fig. 1.5) that followed a modified-Poisson behaviour. At $\sqrt{s}$ = 34.8 and 43.6 GeV (Fig. 1.5), however, they observed significant deviations from this form [13]. In fact, if one attributes a Poisson-like behaviour to the pairwise production of charged particles, one expects a "pair-Poisson" distribution of the form

$$\begin{aligned} P^{pair}(n) &= \frac{(< n > /2)^{n/2} e^{-<n>/2}}{(n/2)!} && n = even \\ &= 0 && n = odd. \end{aligned} \tag{1.6}$$

This pair-Poisson distribution has $D = \sqrt{2 < n >}$, which is considerably broader than the values measured by the HRS and TASSO experiments.

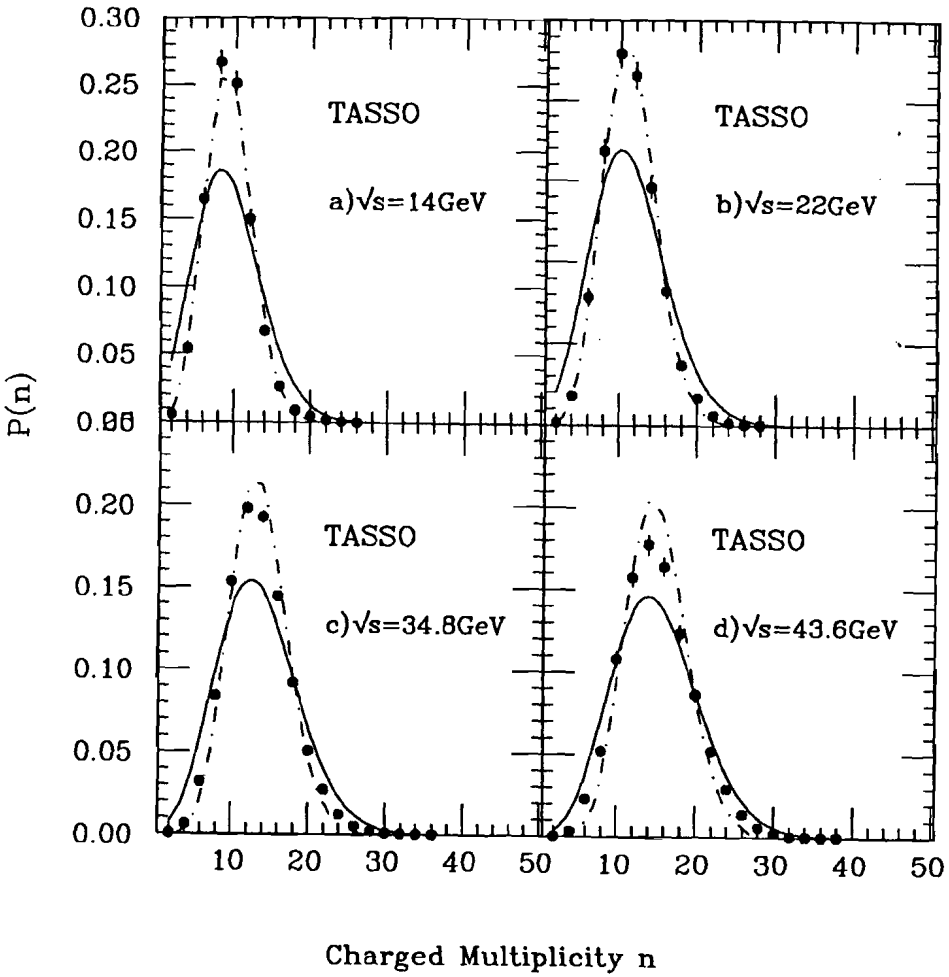

Figure 1.5: The corrected charged multiplicity distribution for the TASSO experiment compared with the modified-Poisson (dash curve), and pair-Poisson (solid curve) distributions.

Gamma Distribution and Negative-binomial Distribution

While the KNO scaling function is usually taken to be a "Gamma distribution",

$$\psi(Z) = \frac{K^K}{\Gamma(K)} Z^{K-1} e^{-KZ} \tag{1.7}$$

where Z = n/ < n > is the scaled multiplicity, it has been observed that multiplicity distributions in high energy hadronic, leptonic and semileptonic processes can be quite well described by negative-binomial distributions [14, 15, 16, 17]. These distributions can be represented in the form

$$P(n, < n >, k) = \frac{k(k+1)...(k+n-1)}{n!} \left(\frac{< n >}{< n > + k}\right)^n \left(\frac{k}{< n > + k}\right)^k \tag{1.8}$$

where k is related to the dispersion D by

$$\frac{D^2}{< n >^2} = \frac{1}{< n >} + \frac{1}{k} \tag{1.9}$$

This function gives KNO scaling (Eq.1.7) in the limit of < n > much larger than k. (Eq.1.8 is an ordinary binomial distribution when k is a negative integer; in the limit of $k \to \infty$, it has a Poisson form.) Negative-binomial distributions are characteristic of cascade-type (or shower) mechanisms for multiparticle production [14].

1.3 Scope of this Thesis

This dissertation reports on a measurement of the charged particle multiplicity for e^+e^- annihilations into multihadron final states which has been obtained with the AMY detector at the TRISTAN storage ring. The data sample consists of more than 3000 events at center-of-mass energies between 50 to 61.4 GeV. Our results have been compared with those of previous experiments and with predictions of various models, including the Lund 6.3 parton-shower model. The thesis is arranged as follows: The first chapter (the current one) is an introduction where the experimental and throretical survey on the charged multiplicity is done. Chapter 2 is a description of TRISTAN and AMY detector facility. Since the analysis presented in this thesis relies exclusively on charged particles tracked in central drift chamber (CDC), we discuss the CDC in greatest detail. The Monte Carlo simulation of AMY detector, the charged particle tracking and the track-selection and

event-selection are also outlined in this chapter. Chapter 3 describes the method that was used to determine the charged hadron multiplicities, and presents a study of the systematic uncertainties in our measurements. In Chapter 4, we present the fully corrected charged multiplicity results, and discuss the energy dependence of the average charged multiplicity, the shape of multiplicity distribution, and KNO scaling. Finally, in Chapter 5, we summarize and discuss our results.

Chapter 2

TRISTAN and The AMY Experiment

In this chapter, the TRISTAN e^+e^- storage ring and the AMY experiment are described.

2.1 TRISTAN

TRISTAN [18](Transposable Ring Intersecting STorage Accelerator in Nippon) is an electron-positron collider facility that consists of four serially connected subsystems: a positron generator, a 400 m long electron linear accelerator (LINAC), an accumulation ring (AR) of 337 m circumference, and a main ring(MR), as shown in Fig. 2.1.

Positrons, generated by bombarding 200 MeV electrons with intensity of 10 mA onto a Tantalum target, are transferred into the LINAC. Electrons and Positrons are accelerated to 2.5 GeV in the LINAC and from which they are transferred to the AR. After the accumulation of a sufficient number of e^- and e^+ bunches, when a current of about 10 mA per beam is reached, the AR accelerates the electron and positron beams up to 8.0 GeV and injects them into MR.

The 3 km circumference MR consists of four straight sections (each 200 m long), housing radiofrequency cavities that provide a total RF power of 25 MW, and four arc sections (each 550 m long). The electron and positron beams, grouped in two bunches (each of length of a few cm) for each particle type, circulate in opposite directions and collide at four intersection points, located at the center of each straight section, where their transverse dimensions are compressed by focusing magnets. Surrounding the collision points are detector systems for studying the

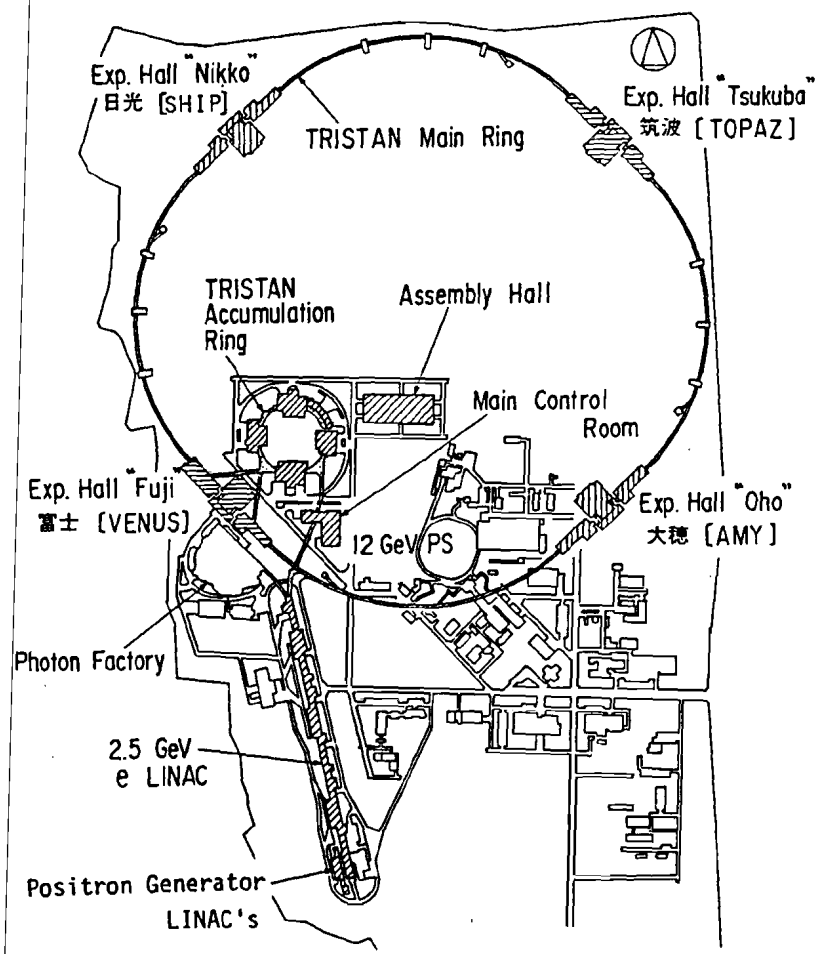

Figure 2.1: The TRISTAN e^+e^- Collider

products of the collisions. Three of the interaction regions contain general purpose detectors, AMY, TOPAZ, and VENUS. SHIP, a specialized experiment designed to find highly ionizing particles, is located in the fourth interaction region. The beam bunches cross every 5 μsec. The typical beam current is 10 mA at the start of data taking and the instantaneous luminosity is typically $1 \times 10^{31} cm^{-2} sec^{-1}$. The time duration of the beam from the peak current ($\sim$ 10 mA) after refilling until the beams are dumped (when the current is $\sim$ 6 mA) is 50 $\sim$ 90 minutes depending on machine conditions. At the collision point the typical bunch size is 2.3 mm wide (in the plane of the MR) by .023 mm high by 1.2 cm long. The energy spread of the beam in the MR is $\sigma_E/E = 1.64 \times 10^{-3}$ (r.m.s), i.e., $\sim$ 50 MeV for 30 GeV beams.

Since the first collisions occurred at a center of mass energy of 50 GeV in November 1986, TRISTAN has steadily increased in energy. In the summer of 1988, superconducting RF cavities were installed in the main ring, replacing approximately half of the conventional RF cavities. This allowed beam energies up to 30.7 GeV.

2.2 AMY

The study of multihadronic final states in e^+e^- annihilation, including high multiplicity and extremely jet-like events, requires a facility capable of detecting particles over close to a 4π steradian solid angle with high efficiency. The AMY experiment has such detection capabilities both for the charged particles and photons over the momentum range available at TRISTAN.

The AMY detector [19], located in the southeast straight section of TRISTAN, is a compact multi-purpose detector optimized for lepton identification. A schematic view of the facility is show in Fig. 2.2. Based on a superconducting 3 Tesla solenoid magnet, it is considerably more compact than other general purpose detectors. The high field allows for high momentum resolution of charged particles, even though the tracking length is small. The small size also allows the use of a thick iron yoke with a large absorption length for strongly interacting particles. This thick hadron filter together with the short decay path enables

good muon identification with relatively low backgrounds from punch-through and decay in flight of pions and kaons. A finely segmented lead-gas sampling electromagnetic calorimeter is located inside the superconducting solenoid. It determines the energy and direction of photons and provides good electron identification and separation between single high energy photons and π^0s. Synchrotron radiation emitted by electrons bending in the 3 Tesla magnetic field gives a unique capability of isolating electrons from charged hadrons. In addition, high luminosity can be obtained by placing focusing quadrupoles close to the interaction point.

Radially outward from the beam pipe, the essential components are: the Inner Tracking Chamber (ITC) and Central Drift Chamber (CDC), which measure the momenta of the charged particles produced in the e^+e^- collisions; the synchrotron X-Ray Detector (XRD), which aids in the identification of electrons; the Barrel Electromagnetic Shower Counter (SHC); the Superconducting Magnet; the Iron Return Yoke. Outside the iron flux return are planar drift tubes and scintillation timing counters for muon identification (MUO). In addition, in the endcap region there are several electromagnetic calorimeters: the Pole Tip Counter (PTC), the Ring Veto Counter (RVC), and the Small Angle Counter (SAC). These provide some particle tracking in the small-scattering-angle region. The PTC has the important function of counting small-angle Bhabha-scattering events, $e^+e^- \rightarrow e^+e^-$, from which the integrated luminosity is determined.

The AMY coordinate system is a right-handed system with z defined to be the direction of the electron beam and y taken as the vertical direction. The polar angle relative to the z axis is θ. Both ϕ and r are measured in the $x-y$ plane, where ϕ is the angle relative to the x axis. These coordinates are shown in Fig. 2.3.

The central detection components of the AMY experiment are the Central Drift Chamber (CDC) and Barrel Electromagnetic Shower Counter (SHC). Since the analysis in this thesis relies exclusively on data from the CDC, the other detector elements are described only briefly.

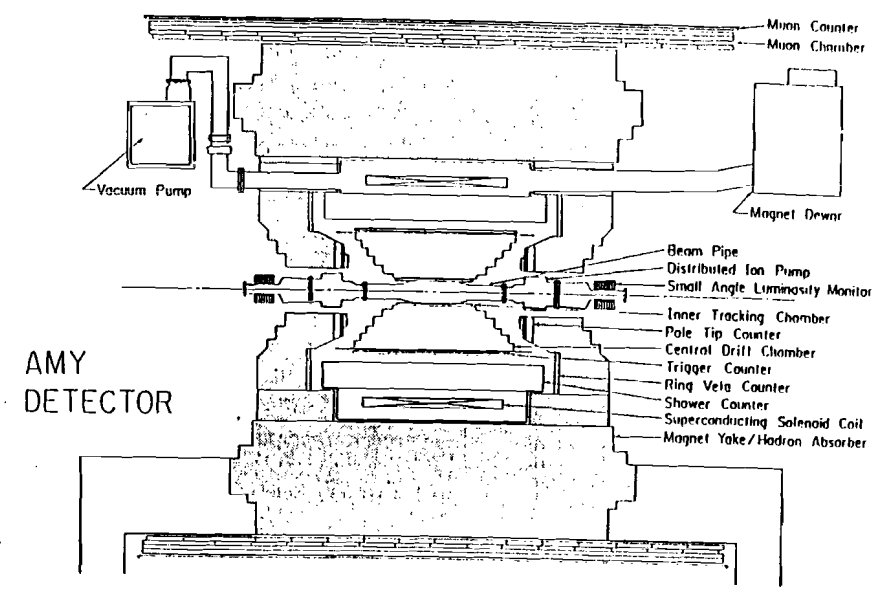

Figure 2.2: The AMY Detector

2.2.1 The Inner Tracking Chamber

The Inner Tracking Chamber (ITC), located just outside of the 10 cm radius beam pipe, is a straw tube design, with a total length of 55 cm in z, and inner and outer radii of 12.2 cm and 14.2 cm. It consists of four layers of 3 mm-radius aluminized plastic tubes, arranged in a close-packed cylindrical geometry parallel to the z axis. Within each tube is a 16 μm-diameter anode wire at 1.7 kV. A 50%Ar, 50%C_2H_6 gas mixture, pressurized to 1.48kg/cm^2 to improve spatial resolution, is used. Position resolution as determined from Bhabha scattering ($e^+e^- \rightarrow e^+e^-$) is 85 μm in $r - \phi$. The ITC does not give information about the z coordinate.

2.2.2 Central Drift Chamber

The momenta of the charged particles was measured by the Central Drift Chamber (CDC). In the 3 Tesla magnetic field, charged particles move in helical paths through the volume of the CDC, creating a trail of ions. The ionization electrons are focussed on to anode wires in the gas volume, where they produce many secondary electrons that are collected on the anode wires. The time between the beam crossing and the first indication of a signal on an anode wire can be translated into the distance of closest approach between the particle that produced the ionization and the anode wire by empirically determined drift functions that depend on the fields and the gas. Because the CDC is in a 3 T field, the paths the ionization electrons take as they approach the anode wire are complex spirals [20]. Helices fit to the trajectory points determined by the CDC are used to infer the curvature of the charged particle's track, and, thus, the component of its momentum perpendicular to the magnetic field.

The CDC, shown in Fig. 2.3, consists of six concentric cylindrical bands of wires. The inner radius of the innermost band is 16 cm. The outermost band has an outer radius of 65 cm, with a length of 180 cm. The CDC provides charged particle tracking in the region defined by $|\cos\theta| \leq 0.87$. There are a total of 40 cylindrical layers of wires, 25 of the layers have wires (axial wires) parallel to the beam direction (the z-axis) for measuring the $r - \phi$ coordinates of trajectory points; the other 15 layers have wires (stereo wires) with a small stereo angle (approxi-

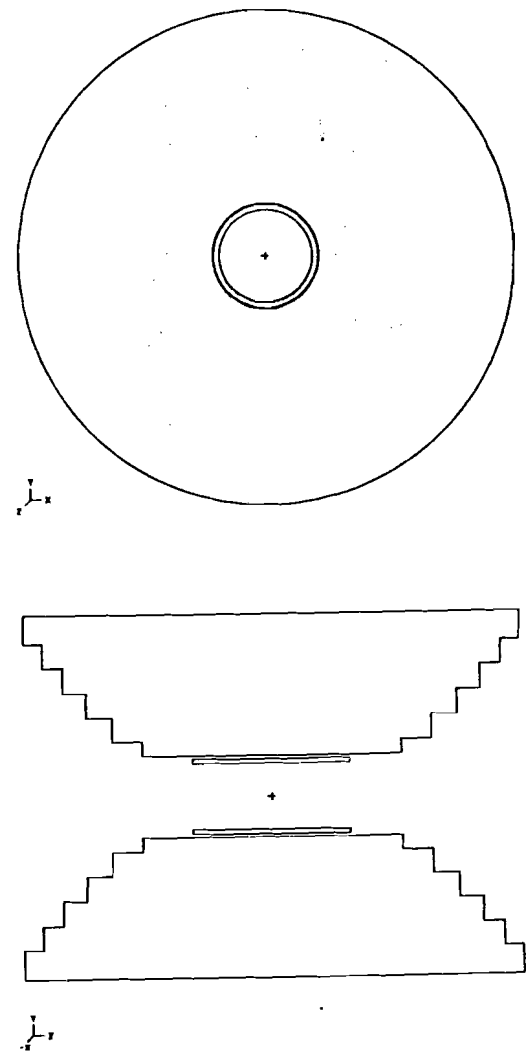

Figure 2.3: The Central Drift Chamber (CDC) of the AMY detector.

mately 5°) relative to the beam direction, allowing small angle stereo measurements of z-coordinates. In each band, there are four axial and three stereo layers, except for the innermost band which contains five axial wire layers only.

Wires are arranged in closed hexagonal cells, each approximately 6 mm in diameter, consisting of one anode wire (either axial or stereo) and six field wires. Anode wires are 20 μm-diameter gold-plated tungsten. Field wires are 160 μm gold-plated aluminum, the use of aluminum minimizes the amount of material in the CDC, reducing multiple-scattering of charged particles. The total number of wires in the CDC is 32072 among which 9048 are anode wires. From 1986 to Spring 1989, HRS gas (89%Ar, 10%CO_2, 1%CH_4) was used in the chamber.

The anode wires are instrumented with current-sensing preamplifiers, having a gain of 8 mV/μA. These are connected through 6 m long twisted pair cables to a post-amplifier and discriminator. The discriminator fires if the current on the anode wires is greater than approximately 1 μA. The output from the discriminator goes through a 25 m cable to a time-to-digital fastbus conversion system which is read out by the AMY data acquisition system.

The band structure allows local determination of track segments within a given band. This provides quick estimates of the multiplicity and momenta of the charged particles for triggering the online data acquisition system, and also facilitates fast, efficient, and precise measurement of the tracks in the complicated events with high multiplicity.

The momentum resolution of the CDC has been measured using Bhabha-scattering events to be $\Delta p_t/p_t = .7\% p_t$, which corresponds to a spatial resolution of 170 μm.

The reliability of our multiplicity determination is enhanced by the relatively small amount of material encountered by charged particles and photons as they emerge from the interaction region. The vacuum pipe of TRISTAN is aluminum with a wall thickness of 1.5 mm. The ITC is constructed of polystyrene and epoxy, and the inner cylinder of the CDC vessel is made of carbon-fiber reinforced plastic. Radially, the material between the interaction point and the first tracking layer of the CDC corresponds to 3.0% of a radiation length (a radiation length is the

thickness of a material required for a high energy electron to lose all but 1/e of its energy via bremsstrahlung) and 0.8% of an interaction length. This relatively thin front end, combined with the high magnetic field, minimizes the number of spurious charged tracks resulting from photon conversions and nuclear interactions.

More details on the CDC can be found in appendix A and ref. [21]. The track recognition programs are described below.

2.2.3 Barrel Electromagnetic Calorimeter

Outside of the CDC is a cylindrical Barrel Electromagnetic Calorimeter (or Shower Counter, SHC), which is used for photon detection and electron identification. The SHC consists of 14.4 radiation lengths of Pb. Its main feature is fine segmentation in both $r-\phi$ and z, allowing for superior position resolution. The SHC is a 220 cm long annular structure of radii 79 cm to 110 cm (Fig. 2.4), it covers the angular region of $|\cos\theta| \leq 0.73$.

Azimuthally the SHC is divided into six identical, independent enclosures, called sextants. Each sextant consists of 20 layers of lead and gas-filled resistive plastic proportional tubes. In the first 15 layers, the lead is 3.5 mm thick. In the last 4 layers, the lead thickness is 7 mm.

To obtain good electron identification and γ/π^0 separation, two orthogonal cathode segmentations are used in the inner and outer radius of each layer of tubes, as shown in Fig. 2.4. The cathode layers consist of thin orthogonal rectangular copper strips etched onto the two PC boards. Ionization avalanches within the tubes induce signals on the cathodes, which are read out by the strips. The inner radius strips are arranged perpendicular to z, providing θ position information; the outer strips are parallel to z, providing ϕ position information. The θ strips are 13.5 mrad (0.77°) wide; the ϕ strips 16.3 mrad (0.93°) wide.

Anode wires are located at the center of the conducting plastic tubes as shown in Fig. 2.4 and operated at 2150 V in a gas mixture of 49.3%Ar, 49.3%C_2H_5, and 1.5%C_2H_5OH.

Signals from the anodes and the θ and ϕ cathodes are read out through FASTBUS analog-to-digital converter (ADC) modules. In addition, the anodes for each

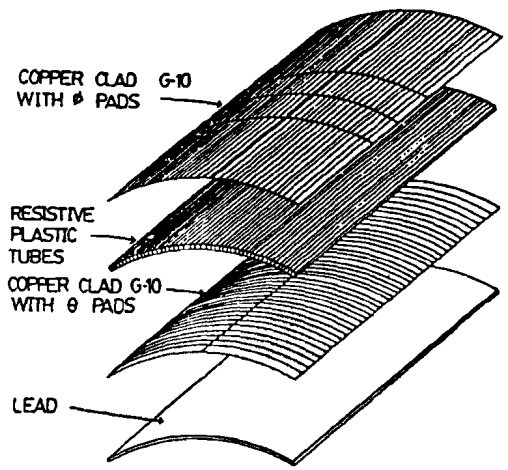

Figure 2.5: The segmentation of cathode pads

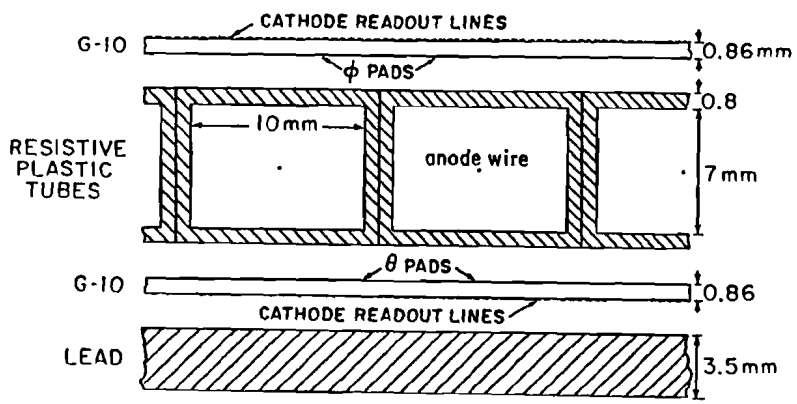

Figure 2.4: The Shower Counter (SHC)

$\sqrt{s}$	a	b	Bhabha energy resolution
52	21.1±4.0	7.1±0.9	11.4±0.2
56	22.6±1.8	7.2±0.5	11.6±0.2
60	35.9±4.2	17.0±0.6	18.5±0.5

Table 2.1: SHC resolution, in form $\sigma_E/E = a \times E^{-1/2} + b$, SHC analysis version 522.

layer are ganged in ϕ, with each gang covering $\Delta\phi = 7.5°$, to provide triggering information. The signals from the last four anode layers are summed and amplified to provide triggering information for minimum ionizing particles (such as μ pairs). The anode output from the first 16 layers is used in other triggers.

The signals from the cathode strips of four consecutive layers are tied together resulting in a total of five ganged layers in the radial direction. This gives five radial samples per SHC cluster in both the θ and ϕ directions.

The energy and position resolution of the SHC has been studied using $e^+e^- \rightarrow e^+e^-$, $e^+e^- \rightarrow \gamma\gamma$, $e^+e^- \rightarrow e^+e^-e^+e^-$, and $e^+e^- \rightarrow e^+e^-\gamma$ events. The energy resolution is $\sigma_E/E = 22.6/\sqrt{E} + 7.2$ %. The spatial resolution, determined from $e^+e^- \rightarrow \gamma\gamma$ events, is $\sigma_\theta \sim 0.3°$ and $\sigma_\phi \sim 0.1°$ (0.4 cm and 0.1 cm at $r = 79$cm) [22].

The SHC was damaged during the summer of 1988. Approximately 20% of the anode wires in sextant 1 and 17% of the anode wires in sextant 6 were destroyed. Data taken with beam energies less than or equal to 28.5 GeV were taken before this damage occurred, those with higher beam energies were taken after. For comparison, the energy resolution below and above $\sqrt{s}$=57 GeV is shown in Table 2.1. Table 2.2 shows the SHC energy resolution sextant-by-sextant for the 60 GeV data.

More details on the SHC can be found in reference [22, 23].

2.2.4 The Superconducting Magnet

The 3 Tesla superconducting magnet coil and iron flux return yoke resides radially outside of the SHC. The direction of the magnetic field is along the $+z$ axis. The coil consists of eight layers of windings situated between $119 < r < 129$cm, with a

sextant	σ_E/E (%)
1	22.0±2.2
2	13.2±0.8
3	18.0±1.3
4	11.2±0.8
5	16.6±1.1
6	26.0±2.0

Table 2.2: SHC resolution sextant-by-sextant, for Bhabha events, SHC analysis version 522.

total length of 154 cm. The current is carried by a Nb/Ti superconducting cable that is embedded in a copper channel, with aluminum added to enhance stability at high fields. It is cooled by a 4.2° K liquid helium bath. Its operating current is 5000 A and its stored energy is 40 MJoules.

The return iron also serves as the hadron absorber for muon identification. Because of AMY's overall compactness, thicker return iron could be utilized, lowering the hadron punch-thru probability. A minimum thickness of 127 cm of iron in the radial direction, together with the material in the SHC and magnet coil, provide an average of 165 cm of iron equivalent (approximately 9.7 interaction lengths) between the CDC and the muon identification system.

More details on the magnet can be found in reference [24].

2.2.5 Muon Chamber

Outside the iron yoke, there is an array of 6 muon chambers (MUO) to detect charged particles penetrating the iron. Each chamber consists of two orthogonal sets of 2-layer drift tubes (muon chambers) and is followed by a layer of scintillator timing counters (muon counters) to provide time information to distinguish muons produced in e^+e^- interactions from cosmic rays. The chamber and the counter system covers the region $|\cos\theta| \leq 0.74$. Muons with $|P| > 3$ GeV penetrate the iron and produce signals in the drift chamber and the scintillator systems. Hadrons, on the other hand, lose their energy through nuclear interactions within the return yoke, and stop before reaching the muon system. A muon chamber track matched to a CDC track is thus the signature of a muon.

The muon chambers are located at $r = 277$ cm at closest approach. The length of the chambers vary from 280 cm to 410 cm in azimuth, and 650 cm in z. Each chamber consists of four layers of 5cm × 10cm aluminum drift tubes. The last two layers are parallel to the z axis, with the tubes offset by 5cm, providing $r - \phi$ coordinate tracking. The first two layers are perpendicular to the last two, providing z coordinate information. The aluminum tube itself forms the cathode. In the center of each tube is a 100 μm-diameter gold plated anode wire. P10 gas, a mixture of 90%Ar and 10%CH_4, is used. The signal is read out through a preamplifier/discriminator card, followed by a FASTBUS TAC, scan-ADC. A muon chamber track is required to have hits in 3 out of the 4 muon drift chamber layers. The muon chamber tracking efficiency for charged particles is 98%, as determined from cosmic ray muons.

The muon counters are located immediately after the fourth layer of drift tubes. The geometrical acceptance of the counters is identical to the chambers. Signals from the scintillators' photomultiplier tubes are read out by a TAC + ADC system and converted into timing information. The scintillators alone provide approximately 15 nsec resolution. Using the muon chamber information to correct for position improves the timing resolution to 2.5nsec ~ 3.5nsec.

The system has a position resolution of approximately 1 mm, but the distance between the track extrapolation and the muon chamber hit position is dominated by the effects of multiple scattering, CDC tracking, and the uncertainties in the magnetic field strength in the iron yoke.

More details on the MUO can be found in reference [25].

2.2.6 The Endcap Detector

The endcap region of AMY contains three detector elements, the Pole Tip Counter (PTC), which covers the region $14.6° < \theta < 26.6°$, the Ring Veto Counter (RVC), covering $26° < \theta < 38°$, and the small angle counter (SAC), covering $2.3° < \theta < 4.0°$. Except for luminosity determinations, the endcap detector elements were not used in this analysis.

The PTC is used to provide precise luminosity measurements, via Bhabha

events, and for tagging small angle photons. The Bhabha rate into the PTC is $\sim$ 1/min. The PTC consists of lead-scintillator sampling calorimeters with a thickness 14 radiation lengths of lead. For measuring the location of showering particles, a gas proportional tube array is located at a depth of 5.7 radiation lengths. The energy resolution is 11% for 28 GeV/c Bhabha electrons. The position resolution is $\sigma_\theta = 0.2°$ and $\sigma_\phi = 1.0°$.

The RVC consists of two lead/scintillator layers and has a total of 3.6 radiation lengths. It is intended to tag particles which travel between the SHC and PTC. The CDC tracks entering in this region are thus identified as electrons or minimum ionizing particles by means of the pulse heights recorded in these counters. The energy resolution for 28 GeV/c electrons is roughly 30%.

The SAC, covering $2.3° \sim 4.0°$ in θ, is made of barium fluoride (BaF_2), and is primarily used to monitor the instantaneous luminosity and beam related background.

More details on the PTC, and on the luminosity calculation, are provided in ref. [26].

2.2.7 The X-Ray Detector and the Trigger Counters

In the initial phases of the AMY experiment, twelve scintillation counters were installed in the space between the CDC and SHC to provide event trigger information and background discrimination. In the summer of 1987, these counters were replaced by the X-Ray Detector (XRD). The XRD is a radial drift chamber filled with a Xenon-Propane gas (95% Xe, 5% propane). It's purpose is to detect synchrotron X-rays emitted by electrons bending in the 3 Tesla magnetic field. This information will be combined with the SHC data give a better electron identification. The data from XRD was not yet available for the analysis reported here.

2.2.8 Trigger Systems and Data Acquisition

In order to be sensitive to as many e^+e^- processes as possible, the trigger requirements for the detector are kept as loose as possible, consistent with the maximum possible 3 Hz. As a result, we typically accumulate approximately 5,000 events/hour, of which only one or two are actual multi-hadron annihilation.

For multi-hadron events, triggers are generated via three quasi-independent systems. The simplest of these requires that an analog sum of the pulse heights from the 48 SHC anode towers exceed a threshold. The threshold, which is typically $\sim$ 3 GeV, is adjusted to produce a trigger rate not exceeding $\sim$0.3 Hz. The second system requires the presence of four or more radial track segments in each of the outer five CDC super-layers. The third system places a weak demand on the presence of CDC track segments but also requires detection of two or more track segments in the ITC. Each system renders a decision in less than 2.0 μs, and the combined trigger rate is less than the 3.0 Hz capacity of the data-logging system. More than 95% of the events in the hadronic sample satisfied the requirements of all three trigger systems.

A computer-controlled FASTBUS system digitizes analog signals from the SHC, PTC, FTC, and ITC, and timing signals from the CDC, ITC, and MUO. Triggers, chamber high voltage control, and environmental monitors are all controlled and monitored by means of a CAMAC system. All the digitized data are read in by a VAX–11/780 computer, where they are temporarily stored. There, various checks are made to monitor operation of the entire detector system. The data are then sent via an optical link to a FACOM M780 computer, where the data format is immediately rearranged for the convenience of later analysis. The data are stored in a cassette-tape library from which it can be subsequently accessed for offline analyses. A schematic of the data aquisition system is shown in Fig 2.5.

The efficiency for triggering on those $e^+e^- \rightarrow \gamma, Z^0 \rightarrow$ hadrons events which also pass the offline cuts has been estimated to be greater than 99% [27]. Therefore, trigger inefficiencies have only a negligible effect on our analysis of hadronic events.

2.3 Monte Carlo Simulation

In the TRISTAN accelerator, an e^+e^- collision may result in the production of as many as a hundred final state particles. The detector is a complex imperfect system. Therefore, it is impossible to calculate analytically the properties of e^+e^-

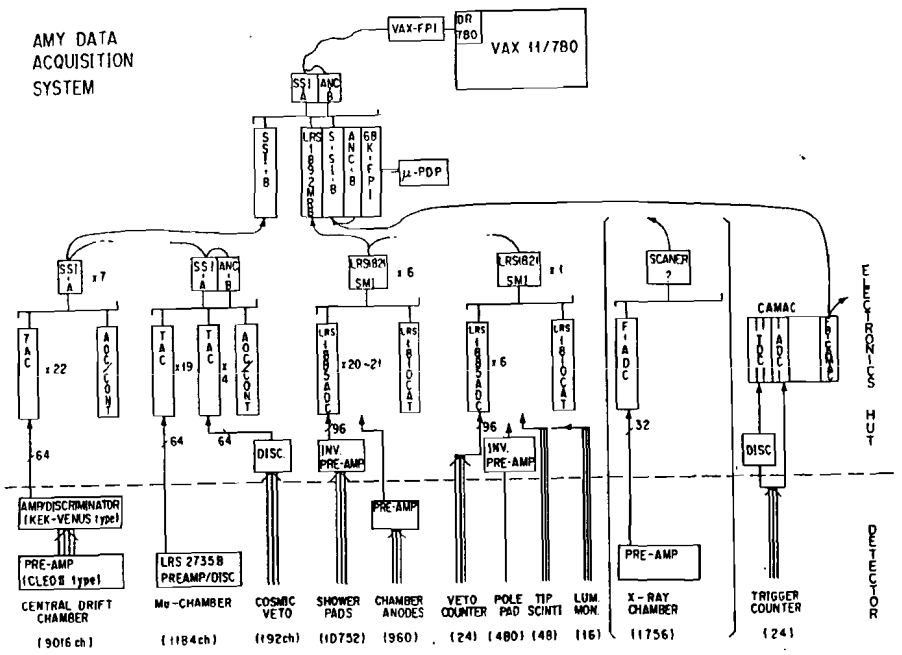

Figure 2.5: AMY's data aquisition system

annihilation events as they would be observed by the AMY detector. Instead, Monte Carlo (MC) simulation methods are used to estimate the detection efficiency and the response of our detector to multi-hadron events and various background processes. There are two stages in the MC simulation of physical processes:

1. Event generation. This includes the production and fragmentation of partons and the decay of short-lived particles produced in the fragmentation process; the energies and directions of the partons are randomly selected according to a probability function derived from QCD. "Events" are generated, i.e., the species and four-momenta of the final state particles are produced by MC methods based on theoretical models. Finally, only electrons, photons, neutrinos, muons and reasonably long-lived hadrons (π^{+-}, K_{+-}, K_L, p, n) remain.

2. Detector simulation. Here we simulate the responses of our detector to the particles generated in the previous stage, formatting the results in the same way as is done for the actual experimental data so that they can be analyzed by the same data analysis programs.

The hadronic event generation and simulation are described below.

2.3.1 Hadronic Event Generation

In general, at very small distance scales, QCD perturbation theory can be used to describe the annihilation of the incoming e^+e^- pair via a virtual γ/Z^0, and the creation of an outgoing quark and antiquark pair. Perturbation theory may be used to describe the subsequent emission of extra gluons. At somewhat larger distances ($c\tau \simeq 1-5fm$), the outgoing quarks and gluons, which are colored, are transformed into color-singlet hadrons; this is called the fragmentation or hadronization process. This transformation reflects the nonperturbative confinement property of QCD, for which we must use phenomenological models in order to bridge the gap between the gross features that can be predicted theoretically and the detailed event structures that are observed experimentally.

Present QCD + fragmentation models can, in general, be divided, with respect to their application of QCD calculations, into two classes: those in which partons

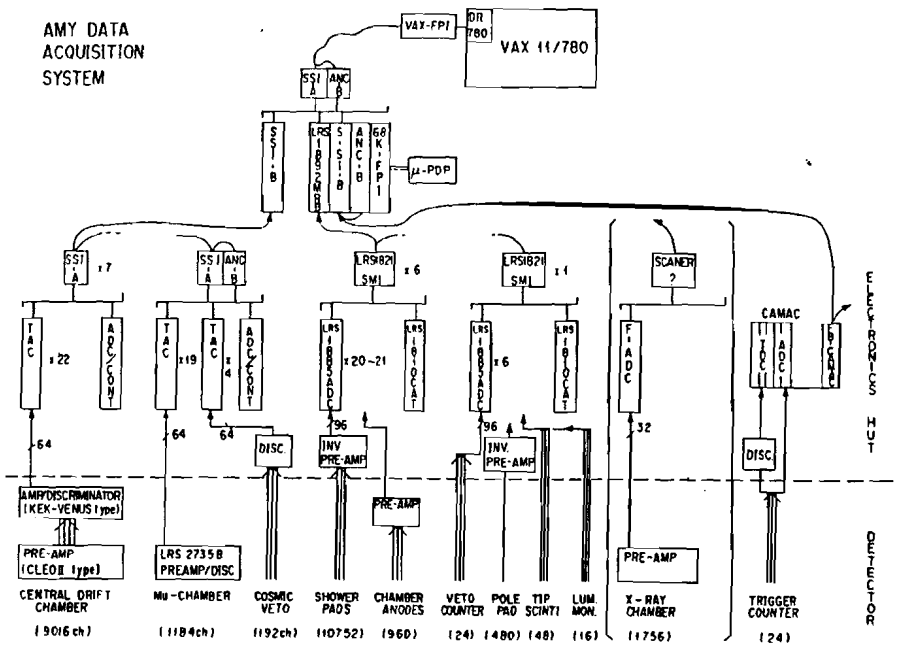

Figure 2.5: AMY's data aquisition system

annihilation events as they would be observed by the AMY detector. Instead, Monte Carlo (MC) simulation methods are used to estimate the detection efficiency and the response of our detector to multi-hadron events and various background processes. There are two stages in the MC simulation of physical processes:

1. Event generation. This includes the production and fragmentation of partons and the decay of short-lived particles produced in the fragmentation process; the energies and directions of the partons are randomly selected according to a probability function derived from QCD. "Events" are generated, i.e., the species and four-momenta of the final state particles are produced by MC methods based on theoretical models. Finally, only electrons, photons, neutrinos, muons and reasonably long-lived hadrons (π^{+-}, K_{+-}, K_L, p, n) remain.

2. Detector simulation. Here we simulate the responses of our detector to the particles generated in the previous stage, formatting the results in the same way as is done for the actual experimental data so that they can be analyzed by the same data analysis programs.

The hadronic event generation and simulation are described below.

2.3.1 Hadronic Event Generation

In general, at very small distance scales, QCD perturbation theory can be used to describe the annihilation of the incoming e^+e^- pair via a virtual γ/Z^0, and the creation of an outgoing quark and antiquark pair. Perturbation theory may be used to describe the subsequent emission of extra gluons. At somewhat larger distances ($c\tau \simeq 1-5fm$), the outgoing quarks and gluons, which are colored, are transformed into color-singlet hadrons; this is called the fragmentation or hadronization process. This transformation reflects the nonperturbative confinement property of QCD, for which we must use phenomenological models in order to bridge the gap between the gross features that can be predicted theoretically and the detailed event structures that are observed experimentally.

Present QCD + fragmentation models can, in general, be divided, with respect to their application of QCD calculations, into two classes: those in which partons

are generated following leading-logarithm parton-shower (PS) evolution and those in which partons are produced according to QCD matrix elements (ME). Fragmentation of the partons into hadrons follows, usually employing one of three models: independent fragmentation (IF), string fragmentation (SF), or cluster fragmentation (CF).

Because of their complexity, fragmentation models are now almost exclusively implemented via Monte Carlo techniques in computer programs. In this analysis, we use two of the most widely used QCD + fragmentation model programs: the LUND JETSET program Version 6.2 [28], incorporating matrix element calculations [29] with string fragmentation [30], and the Lund parton-shower model Version 6.3 [31]. Some of the essential features of these models are briefly discussed below.

The Lund Matrix Element Model

QCD matrix element calculations for the production of up to four-parton final states ($e^+e^- \to q\bar{q}$, $q\bar{q}g$, $q\bar{q}gg$), calculated to first and second order in α_s, are used by this model. To first order, the model uses

$$\alpha_s(Q^2) = \frac{12\pi}{(33 - 2n_f)\ln(Q^2/\Lambda^2_{\overline{MS}})}$$

where n_f is the number of active flavors and $\Lambda_{\overline{MS}}$ is one of the parameters of the model. It has been experimentally observed that the Lund matrix element model, which allows states with at most four partons, fails to reproduce the rates for four-jet-like events [32, 33, 34]. While second order matrix elements appear to be sufficient at low energies, this deficiency becomes evident at PETRA and PEP energies. Because of the complexity of the third order calculations, programs which include complete sets of higher order QCD contributions sections are not available.

Following parton generation, hadrons are formed according to a string fragmentation (SF) scheme [30]. A color-triplet "string" is stretched between the final quarks and is allowed to break by forming additional quark pairs. Gluons are treated as kinks on the string between the quark ends with associated energy and momentum, and are therefore attached to two strings corresponding to the gluon's

double color charge. The longitudinal momentum component relative to the jet axis of the final state hadrons formed in the fragmentation process is distributed according to the symmetric fragmentation function

$$f(z) = (1 - z)^a/z \times \exp[-bm_T^2/z]$$

where m_T is the transverse mass of the hadron ($m_T^2 = m^2 + P_T^2$) and z is the fraction of the primordial parton energy it carries. Each primary quark is assigned a transverse momentum according to a Gaussian spectrum $\sim \exp(-P_T^2/\sigma_q^2)$.

The Lund Parton-Shower Model

To compensate for insufficient knowledge of the higher order contributions to multijet cross sections, the parton shower method generates showers of quarks and gluons through a cascade-like process using a leading-logarithm approximation (LLA). In this method, each parton branches into two partons ($q \to qg$, $g \to gg$, $g \to q\bar{q}$) with a calculated probability, resulting in the development of showers of partons. This is continued until the virtual mass of each parton reaches a certain cut-off mass, taken to be 1 GeV/c² for this analysis.

This treatment of multijet configurations is incorporated into the program JETSET 6.3, and is known as the Lund parton-shower (PS) model. The Lund PS is one of the more commonly used shower models, and it contains an option for including soft gluon interference effects. At the end of the parton generation, the string fragmentation process, described in the previous section, is employed. Thus, the model also uses the string fragmentation parameters.

These models are incorporated into Monte Carlo computer programs that generate hadronic events; these are used for evaluating the detector's response for hadronic events. The accuracy of this procedure is checked by comparing various physical quantities in generated events with those measured in real events. Even so, different models that reproduce the general properties of the real data may, possibly, give different values for the response. This is due to the various uncertainties in the

event generation schemes (e.g. matrix element or parton shower) and ambiguities in the fragmentation models. Thus, there is a systematic error associated with the evaluation of the detectors response; an analysis of this is given in reference [27].

We use the Lund MC program (Jetset version 6.3) [31], or Lund 6.3 for short, with the parton shower scheme and the SF model as our standard MC generator of hadronic events. The default values [35] are used for the phenomenological parameters in the code. The generated events describe the particle distributions (Fig. 2.6 and Fig. 3.1 in the next chapter) and global event properties reasonably well [36].

2.3.2 Detector Simulation

Particle Propagation through the Detector

The event simulation program models the interactions and decays of the particles that are generated by the event generator and the response of the various detector components using our best knowledge of the detector system. In the detector simulator, each particle is "swum" through the detector in small steps. At each step, the particle is allowed to decay or undergo an interaction according to the known probabilities, using MC techniques. A charged particle loses its energy through ionization processes in material and may change its direction because of multiple Coulomb scattering. Its trajectory is bent as it moves under the influence of the magnetic field and electrons can emit bremsstrahlung photons. Photons may convert into an e^+e^- pair in material; hadronic particles may undergo nuclear interactions. All these probabilistic processes are included in the simulation.

Electromagnetic showers initiated by photons and electrons inside dense material (e.g. the SHC or the PTC) are developed by the simulation program EGS4 [37]. Hadrons may cause hadron showers inside the material of the detector, which are treated by the program package GRANT [38].

Inside the CDC, as a charged particle passes through one of the wire cells, the closest distance of the particle to the sense wire is determined and converted into a drift time by using the nominal drift velocity of the ionization electrons. This drift distance is smeared by the known spatial resolution of the chamber. If more

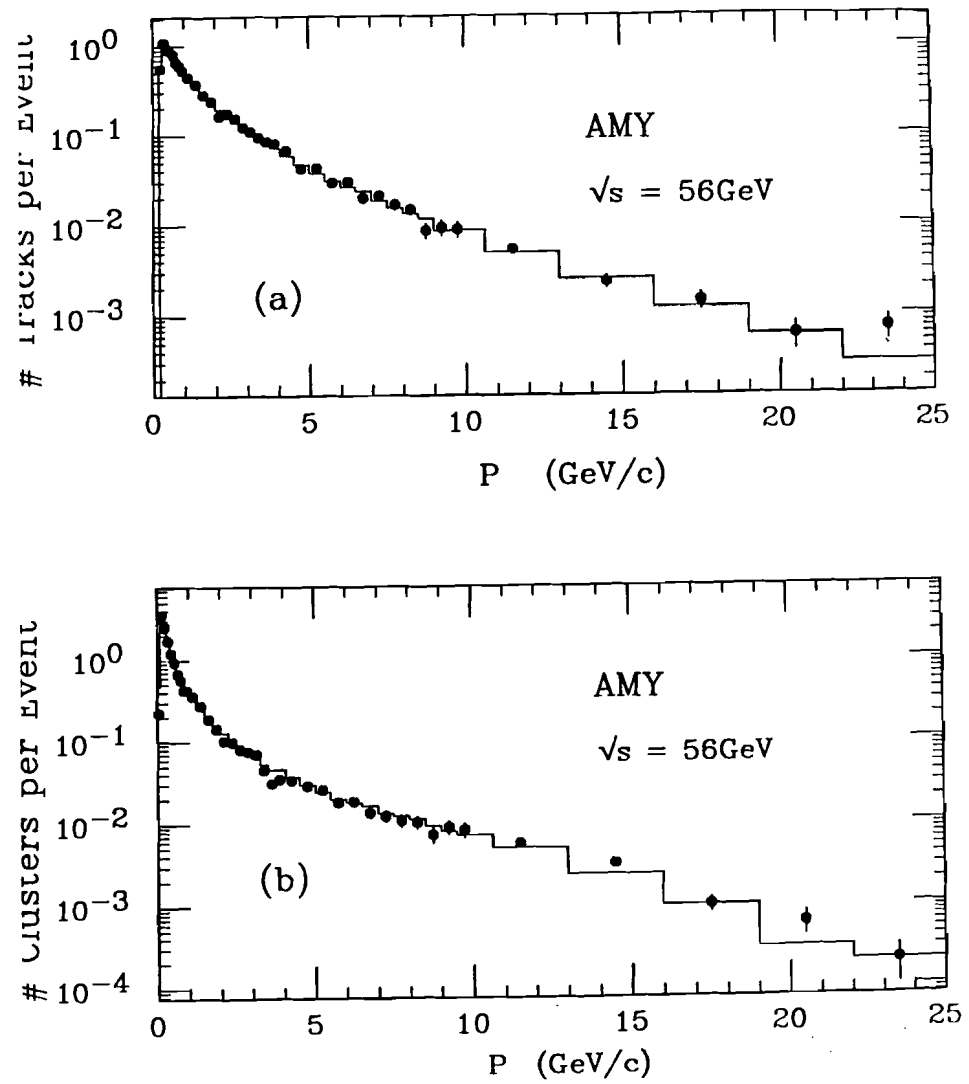

Figure 2.6: The momentum distributions of charged particles (a) and of neutral particles (b) for the real data (points) and the data generated by Lund 6.3. (histogram) for 56 GeV.

than one charged particle passes through the same cell, only the shortest drift time is recorded.

Inside the SHC, the EGS4 code is used to develop electromagnetic showers and to calculate the deposited energies. These energies are converted into ADC counts for the corresponding cathode strips and anode wires according to the calibration data of the SHC.

All the detector signals thus obtained are formatted in the same way as the real data, and are subjected to the same analysis programs that analyze the real data.

CDC Smearing

In the case of real experimental data, there exists a width in the drift- time-to-distance relation of CDC [39]. For a given drift-time, the width of this distribution is a measure of the resolution. In the case of Monte Carlo simulated events, however, the drift distance is known exactly and the drift time is deduced from the time-to-distance function. In order to make the results of the MC simulation reflect the actual case, we have to smear the MC drift distances. Two kinds of smearing methods have been employed. The first (and simplest) one assumes a Gaussian distribution with fixed value of 250 μm spatial resolution. However, the distribution of residual of drift times for the experimental data is not purely Gaussian; it has a momentum dependence and a tail. Fig. 2.7 shows the CDC time residual distribution of $\sqrt{s}$ = 56 GeV data. Thus, we devised a second method where we add a long tail to the Gaussian resolution distribution and use different spatial resolutions for different momentum ranges of the charged tracks. The values used are shown in Table 2.3. Smeared values are allowed to extend to eight standard deviations. The chamber efficiencies, which are assumed to vary from layer to layer and depend on the track's position in each cell, are also taken into account. The parameters of the simulator are tuned according to the real data. The time residual distribution of simulated MC data, using the second smearing method, is compared to that of the real data in Fig. 2.7.

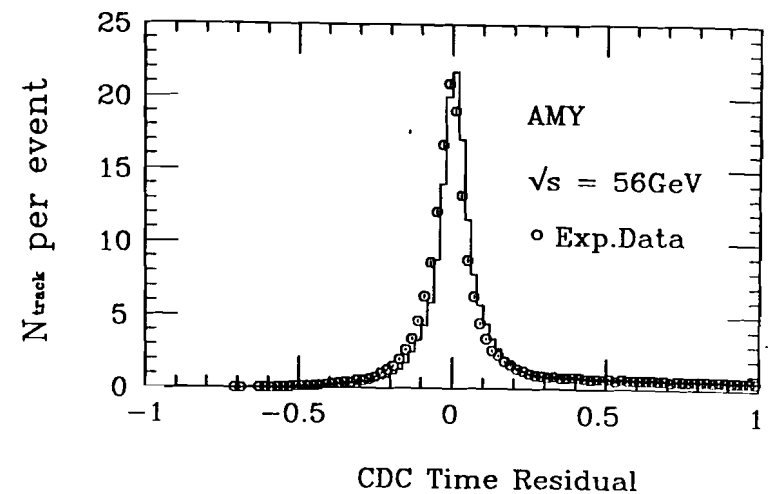

Figure 2.7: The CDC time residual distribution for experiment data (points) and MC simulation (histogram).

Track P (GeV/c)	σ (μm)
P < 0.4	324
0.4 < P < 1	267
1 < P < 3	253
3 < P < 8	195
P > 8	179

Table 2.3: CDC smeared resolution parameters.

2.4 Charged Particle Track Reconstruction

2.4.1 Tracking Program

A charged particle moving through the CDC follows an approximately helical path. The three-momentum of the particle can be determined from the curvature and inclination angle of the tracks. Two offline programs, ACE [40] and DUET [41], are used to recognize tracks among the hit wires in the CDC and fit them to helices.

ACE is a program devised by T. Mori of the AMY group that is specialized to the particular geometry of the AMY CDC. Initially, the hit axial wires are scanned and for each hit wire on the innermost layer (or next to the innermost) of a band, neighboring wires in the other layers of the band are searched for hits. At least 3 hits, each hit in a different layer, are required and used to make an approximate track vector, which gives the position and direction of the track at the position of the band. This allows for one (or two in the case of band 1) missed hits per band, reducing our sensitivity to chamber inefficiency and hit sharing by two close tracks traversing the same wire cell. Using the assumption that the track is a circle passing through the origin, the track parameters C (the curvature of the track circle, defined as an inverse of its bending the radius) and ϕ_o (the azimuthal production angle) are calculated from the position and direction of the vector. All the track vectors that are part of the same track should have the same values of C and ϕ_o. ACE can find complete tracks very quickly by looking for clusters of vectors from different bands in a C vs ϕ_o scatter plot. ACE is very fast, it takes less than 20 msec per track for a typical multihadronic event on a FACOM M-382 computer.

The second program, DUET, was devised for the CLEO detector at CESR e^+e^- storage ring, and does a more elaborate search for tracks. By modifying and adding some routines to the code, this program was adjusted for tracking in the AMY CDC. In this program, a "Link-and-Tree" algorithm developed by Kowalski and Cassel [42], is employed. This is exhaustive search method that is not biassed toward tracks that come from the origin, and is faster than a more conventional "Road" method. At the price of providing higher quality tracking, DUET consumes a considerably more CPU time than ACE. Therefore, DUET is

used only on the events that are selected based on the results of ACE. In these events, it takes the tracks found by ACE, refines them, and also tries to reconstruct missed tracks.

More details on AMY charged particle tracking can be found in reference [40].

2.4.2 Track Reconstruction Efficiency

The track reconstruction efficiency was studied using Monte Carlo simulated events where we know how many final state charged particle were produced. The track reconstruction efficiency was obtained by matching each individual reconstructed charged track with a generated charged track. In this calculation, if more than one reconstructed tracks match to a single MC track, the reconstructed track with more hits is chosen. Matching is established only if more than half of the hits of the reconstructed track belong to one MC track.

Track Density Parameter: R_{mix}

For each CDC track with p_t >0.8 GeV, we examine each layer of the CDC to see if another charged particle crossed the same or neighboring CDC cells as those crossed by the particle in question. We define a parameter R_{mix}, which is used to measure the track density, as the number of wires hit by the particle that are also hit by another particle, or have a hit neighboring cell, divided by the total number of cells crossed by the particle, i.e.

$$R_{mix} = \frac{\text{(No. of hits with adjacent } \pm \text{ 2 wires fired)}}{\text{Total No. of hits of this track}}.$$

This serves as a measure of the level of isolation of each track. If $R_{mix} = 0$, the particle is well isolated from the rest of the tracks in an event; if $R_{mix} = 1$, one or more tracks have very similar trajectories. In the case of siumulated MC events, we can determine R_{mix} both from the generated information, which we call R^{gen}_{mix}, and from the observed data only, which we call R^{obs}_{mix}. For the real data, we only can determine R^{obs}_{mix}.

Fig. 2.8 is the observed distribution of R^{obs}_{mix} for all tracks with momentum above 0.8 GeV/c. Here, there is little apparent difference between the Parton

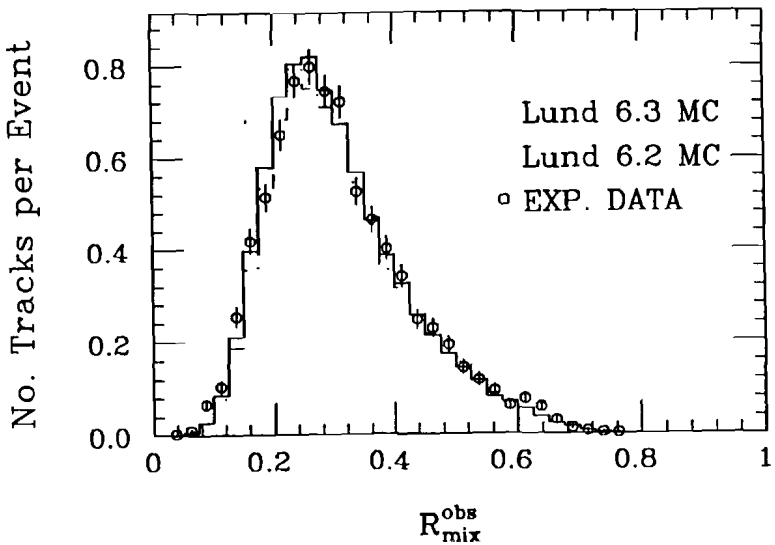

Figure 2.8: Distribution of R^{obs}_{mix} for the data and simulated MC events. The solid line (dashed line) indicates the Parton-Shower (Matrix-Element) model.

Shower (solid line) and Matrix Element (dashed line) MC models. Both reproduce the observed data resonably well, indicating that the MC reliably models the track finding in the detector.

Isolated Tracks

An isolated track in the MC simulated data is defined as one that satisfies the following requirements:

- Transverse momentum p_t greater than 0.8 GeV.
- $0 < R^{gen}_{mix} < 0.04$, this means only two adjacent wires fired or missed along the track trajectory.
- $\Delta\phi, \Delta\theta$ between the closest track greater than 5°.

The track reconstruction efficiency for isolated tracks was determined from the Monte Carlo simulated events to be 99%.

Tracks Within a Jet

Sometimes, however, tracks in tightly collimated jets can be missed. For tracks within jets, the reconstruction efficiency was computed as a function of R^{gen}_{mix}. Fig. 2.9 shows the variation of the reconstruction efficiency as a function of R^{gen}_{mix}. For large values of R^{gen}_{mix} the efficiency is 87%. This shows that missed tracks are almost always lost because of confusion with other nearby tracks.

The tracking efficiency in hadronic events is displayed as a function of the transverse momentum and the polar angle of the tracks in Fig. 2.10 and Fig. 2.11. There is a cut-off for transverse momenta lower than 0.2 GeV/c, in which case the particles barely enter the CDC; particles with transverse momenta of 0.4 GeV/c and above traverse the entire radial extent of the chamber. Fig. 2.10 a) shows that the efficiency reaches the plateau of 94% at p_t = 0.4 GeV/c. From Fig. 2.11 we can see that for all transverse momenta the efficiency depends weakly on the polar angle of the track for values of θ that are greater than 36°.

2.5 Hadronic Event Selection

The data used for this analysis were taken at $\sqrt{s}$ = 50 to 61.4 GeV. Luminosities are listed in Table 2.4. A total luminosity of 29.6 pb^{-1} was accumulated at these energies from November 1986 through August 1989.

2.5.1 Charged Track Selection

The crucial component of our measurement of charged multiplicity is the reliable reconstruction of charged tracks in the CDC. Track candidates were required to have:

- At least eight axial and five stereo hits which could be well fitted to a helix. The small number of hits required, in comparison to the total number possible, helps keep the track reconstruction efficiency high, particularly for

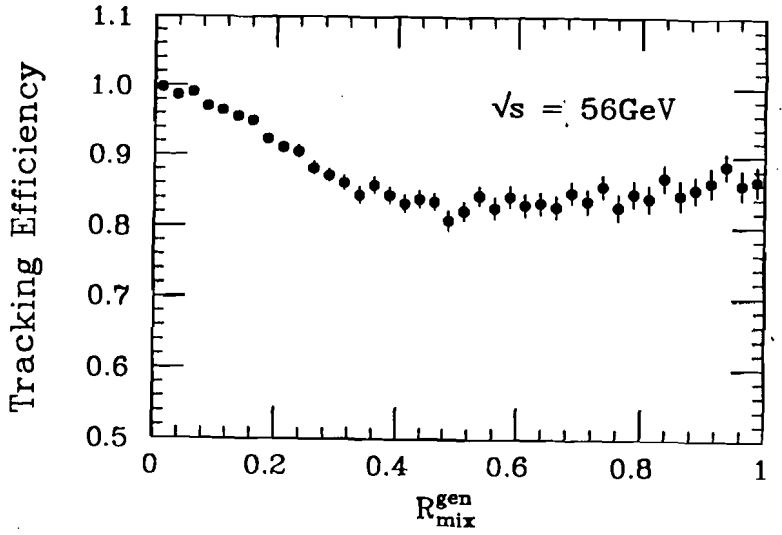

Figure 2.9: The track-reconstruction efficiency as a function of R_{mix}.

$\sqrt{s}$ (GeV)	$\int \mathcal{L} dt$ pb^{-1}
50	0.636 ± 0.016
52	3.976 ± 0.043
55	3.266 ± 0.039
56	5.993 ± 0.053
57	4.398 ± 0.046
60	3.549 ± 0.044
60.8	3.494 ± 0.051
61.4	4.323 ± 0.054

Table 2.4: AMY luminosities for given center-of-mass energies. Errors are statistical only.

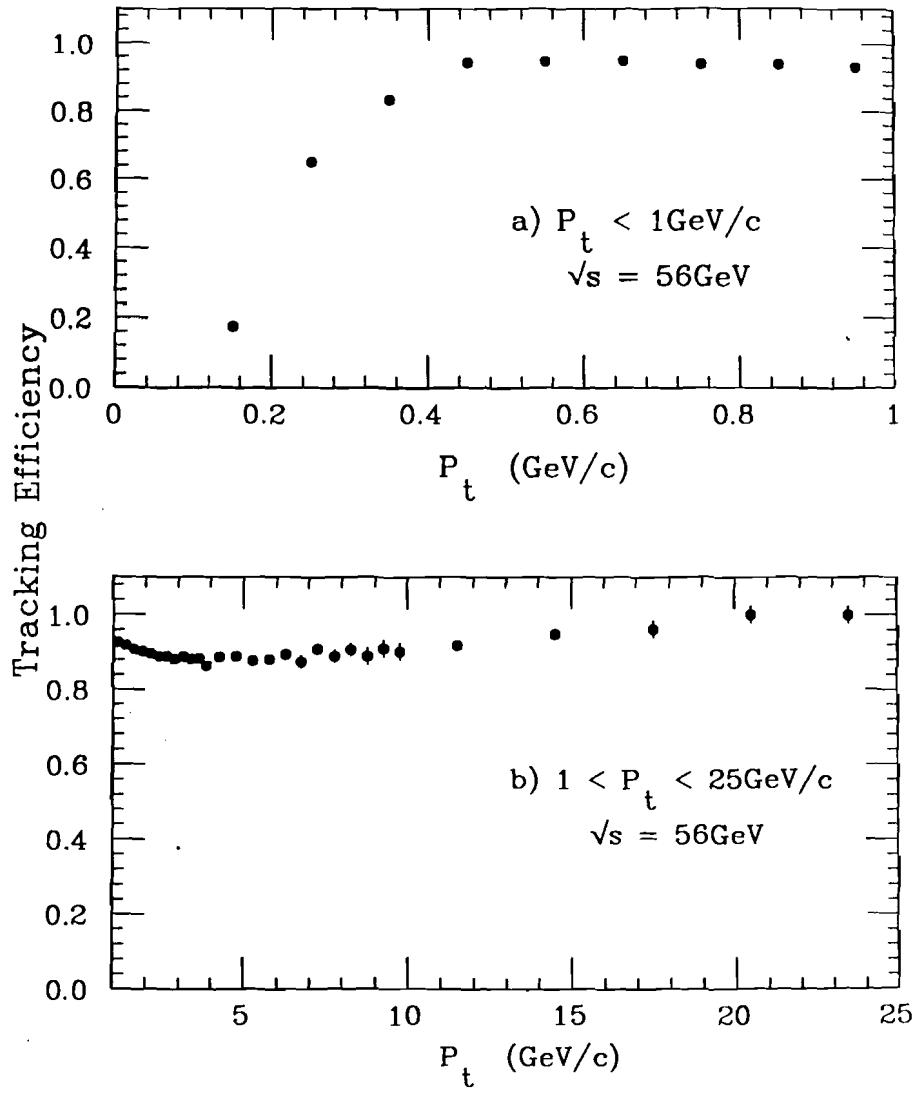

Figure 2.10: The track-reconstruction efficiency as a function of the transverse momentum.

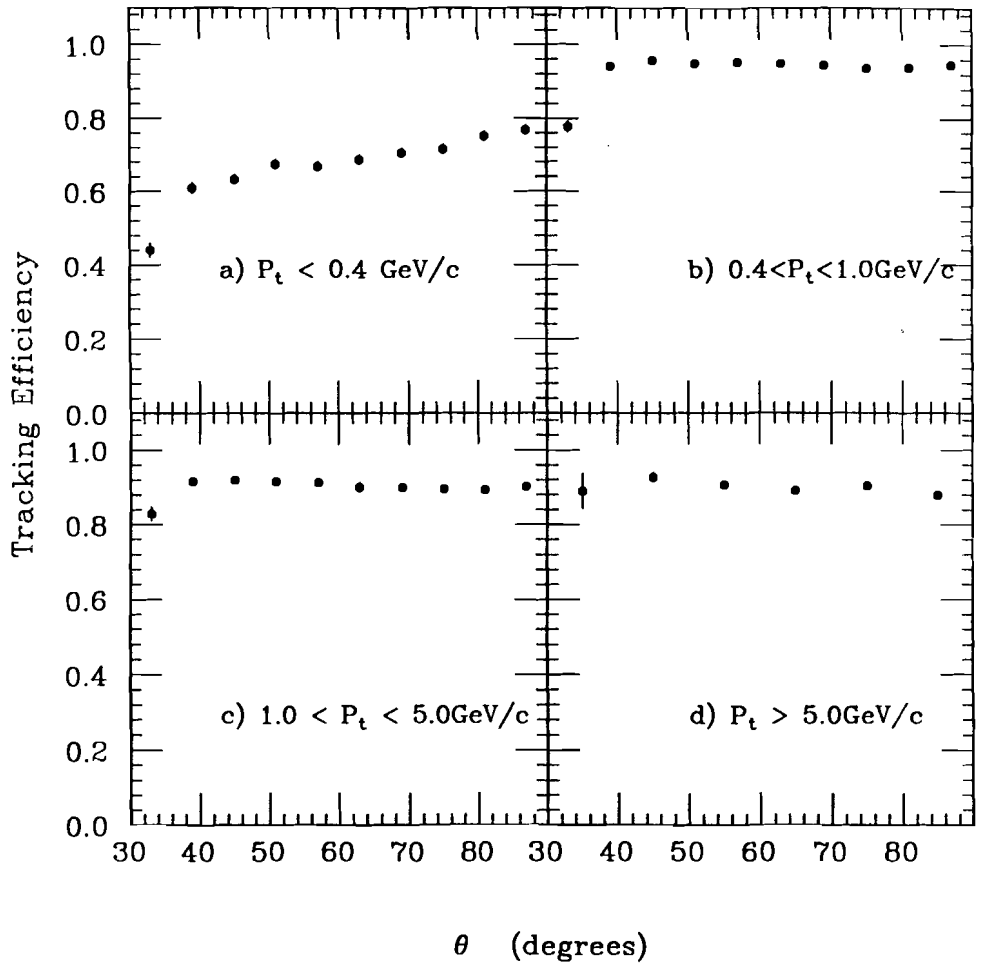

Figure 2.11: The track-reconstruction efficiency as a function of θ, the polar angle with respect to the e^+e^- beam direction.

particles with low momentum and those that are inside tightly collimated jets.

- Each track was required to originate in a cylindrical fiducial volume, centered on the interaction point, with a 5 cm radius in the plane (r, ϕ) transverse to the beam direction, and a length of 30 cm along the beam direction (z).
- A polar angle cut of $|cos\theta| < 0.85$, ensured that high momentum tracks traversed all forty CDC layers.
- The momentum of each charged track was required to be greater than 0.2 GeV/c.
- The fit quality of the reconstructed charged track was required to be $\chi^2 \leq 8$ in the (r,ϕ) view and $\chi^2 \leq 6$ in z view.

Charged particles originating from K^0_s, Λ^0, and heavy meson and baryon decays are included as primary charged particles.

A "good" SHC cluster is one with energy greater than 0.2 GeV and less than 95% of its energy deposited in only one of the five longitudinal layers of the SHC. In order to avoid double counting of a charged particle by the CDC and the SHC, a SHC cluster with energy less than 1 GeV is not regarded as "good" if its position matches with a CDC track within 2°. High energy SHC clusters ($E_{SHC} > 1$ GeV) that match with CDC tracks are either electrons, γ rays accidentally overlapped by charged hadrons, or hadrons that interact in the material of the SHC. Because discrimination of electrons from γ-overlapped hadrons or interacting hadrons depends on the details of our electron identification algorithm, we decided to allow for double counting for $E_{SHC} > 1$ GeV. It was found from Monte Carlo studies that this does not effect the results of event selection; the number of selected events changes by only 0.2~0.3 % between using and not using the double counting.

2.5.2 Hadronic Event Selection

Despite the trigger requirements, many uninteresting events are recorded. These events include such things as beam-wall, beam-gas events (e nucleus $\rightarrow$ e hadrons),

and cosmic ray events. Other events which are recorded have some interest, but not for this analysis. These include interactions such as lepton-pair-production events ($e^+e^- \rightarrow e^+e^-$, $\mu^+\mu^-$, $\tau^+\tau^-$), photon-pair-production events ($e^+e^- \rightarrow \gamma\gamma$), higher-order QED events (such as $e^+e^- \rightarrow e^+e^-\gamma$, $e^+e^-e^+e^-$), two-photon-induced hadronic events ($e^+e^- \rightarrow e^+e^-$ hadrons), etc.

For the convenience of the many physicists doing many different kinds of analysis, the data, after undergoing a preliminary offline analysis, are divided up into several not-mutually-exclusive files. An individual physicist, instead of studying the entire raw data sample, only has to use the file containing that subset of the data most relevant to his/her analysis. This method saves both human and computer time. The base files used for the results reported here were AMY's "hadronic data files". Events in these files pass a series of cuts designed to select $e^+e^- \rightarrow \gamma, Z^0 \rightarrow$ hadrons events, while rejecting all other kinds of events. A thorough description of the selection procedure for the hadronic data files can be found in ref [27].

In order to reject background events while keeping most of the hadronic events in the sample, the following "hadronic event cuts" are imposed:

- At least five well reconstructed charged tracks;
- Total SHC energy, defined as the sum of the energies of all SHC clusters, is greater than 5 GeV (except for the 50 and 52 GeV data samples, where this cut was set at 3 GeV);
- The visible energy, E_{vis}, defined as a sum of absolute momenta (or energies) of all the "good" CDC and SHC particles ($E_{vis} = \sum_{i=CDC} |P^i| + \sum_{j=SHC} E^j$), greater than one half of the total center-of-mass energy;
- The momentum imbalance, P_{bal}, the sum of the z-components of the three-momenta of all the "good" CDC and SHC particles ($P_{bal} = \sum_{i=CDC} P^i_z + \sum_{j=SHC} E^j \cos\theta_j$) that is no more than 40% of the visible energy.

Radiative Bhabha events $e^+e^- \rightarrow e^+e^-\gamma$ and $e^+e^- \rightarrow \tau^+\tau^-$ events, which only rarely have a charged multiplicity higher than four, are effectively eliminated by the

first cut. The third cut rejects almost all beam-wall and beam-gas events (for these, the total energy cannot exceed the beam energy) and most of the $\tau^+\tau^-$ and two-photon events. The fourth cut ensures that there is no large energy leakage into the beam direction, eliminating those events with high energy initial-state radiation photons near the beam directions, and further removes two-photon events.

Computer displays of events that pass these cuts are then scanned by physicists. A very small number of obvious cosmic-ray, beam-gas, and radiative-Bhabha events are removed from the file (less than 2% of the events are removed).

From the z-vertex distribution obtained with the requirements on z relaxed, we deduce that the contamination from beam-gas collisions is less than 0.3%. Monte Carlo simulations indicate that contaminations from $e^+e^- \rightarrow \tau^+\tau^-$ and two-photon processes ($e^+e^- \rightarrow e^+e^-$ + hadrons) are 0.6-0.9% and 0.6-0.7%, respectively, depending on the beam energy [27].

In order to restrict our multiplicity analysis to those events for which the track acceptance is high, we further require that the polar angle (θ_T) of the thrust axis of each event, determined from the charged particles alone, be such that $|cos\theta_T| < 0.70$.

A total of 2740 events pass these selection criteria in our 29.6 pb^{-1} data samples. Using Monte Carlo methods, we have found that 55% of five-flavor events pass the hadronic event selection criteria.

Chapter 3

Determination of the Charged Hadron Multiplicity

For a typical $e^+e^- \rightarrow$ hadrons event, not all of the produced final state charged particles are observed. Corrections have to be made to obtain the true charged hadron multiplicity from the observed one. In this chapter we describe the method by which the charged hadron multiplicity is obtained.

3.1 Observed Multiplicity Distribution

For a hadronic event, the observed multiplicity is defined as the number of CDC tracks which pass the charged track selection criteria. The observed charged hadron multiplicity distribution for the 56 GeV data sample is shown in Fig 3.1 (a). The corresponding distribution for the simulated Lund 6.3 events is plotted as a histogram. The agreement is quite good.

3.2 Corrections

3.2.1 Origin of the Correction

In order to extract the true multiplicity distribution, it is necessary to correct for the loss of charged particles due to incomplete acceptance and imperfect track-finding. In addition, QED initial-state radiation [43] decreases the center-of-mass energy of the annihilating e^+e^- pair, and further reduces the observed charged multiplicity. On the other hand, the conversion of γ-rays to e^+e^- pairs and the nuclear interactions of hadrons in the material of the inner part of the detector can generate extra charged particles. The data are corrected for all of these effects.

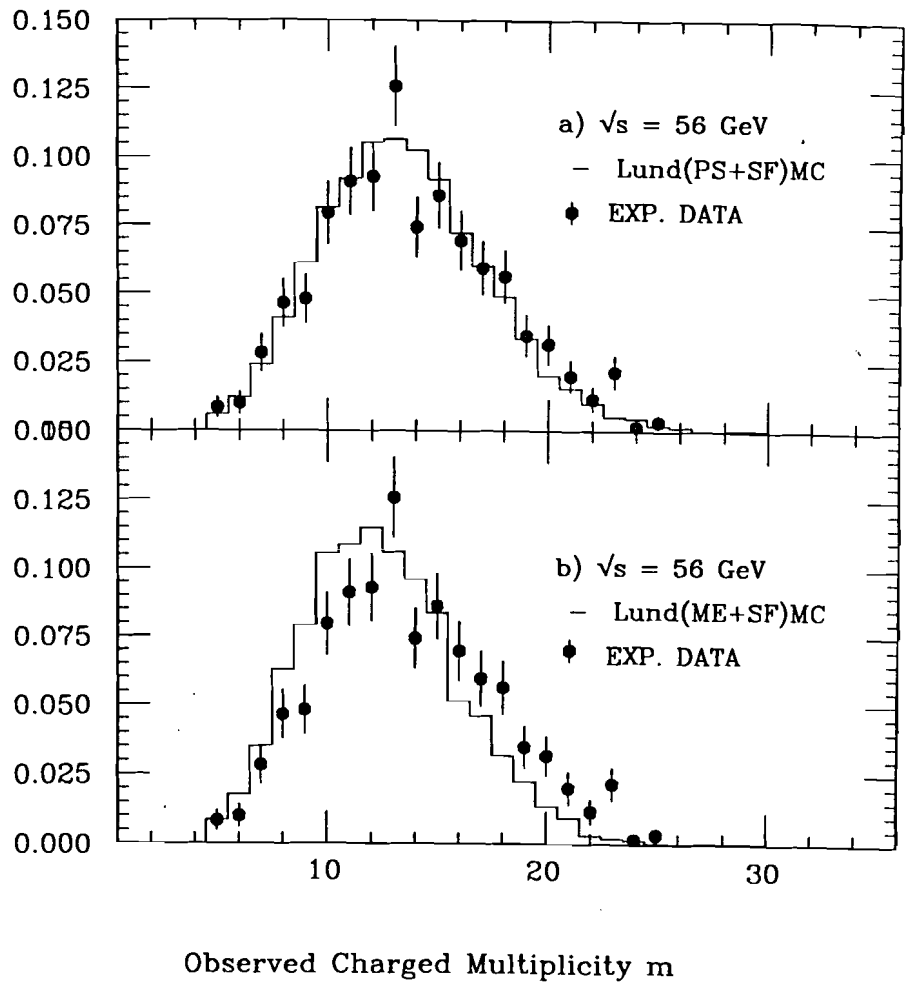

Figure 3.1: The observed charged hadron multiplicity distribution at center-of-mass energy equals to 56 GeV compared with simulated events generated with (a) the Lund 6.3 and (b) the Lund 6.2 Monte Carlo event generators.

3.2.2 Correction for Detector Effects

The correction procedure was based on Monte Carlo simulated events generated using the Lund 6.3 parton-shower model. The first step was to correct for detector effects.

True Multiplicity

We defined the true multiplicity of an event as the total number of charged particles generated by the Monte Carlo, including the effects of QED initial-state radiation, at any angle and momentum. As is customary for these measurements, we let all of the strange hyperons, K^0_s, charm, and beauty particles decay at the generator level, and, thus, charged particles among their decay products are included in the true multiplicity. So, charged particles from $K^0_s \rightarrow \pi^+\pi^-$ ($c\tau$ = 2.675 cm) and $\Lambda^0 \rightarrow p\pi^-$ ($c\tau$ = 7.89 cm) are included in the true charged multiplicity, even though there is some chance for the decays to occur far from the vertex. In the Lund 6.3 model, the average number of charged particles per event from $K^0_s \rightarrow \pi^+\pi^-$ and $\Lambda^0 \rightarrow p\pi^-$ (plus $\overline{\Lambda^0} \rightarrow \bar{p}\pi^+$) are 1.14 and 0.28, respectively.

Correction Matrix

The frequency for events generated with n tracks to be observed with m tracks was obtained after applying the analysis cuts to reconstructed simulated events. This was used to determine a correction matrix for use in obtaining the true multiplicity distribution from the observed distribution.

The element A(n, m) of the correction matrix is defined to be the fraction of those events with m observed tracks that have a true multiplicity n,

$$A(n,m) = \frac{\text{No. of events with } n \text{ tracks generated and } m \text{ tracks observed}}{\text{No. of events with } m \text{ tracks observed}}.$$

In A(n, m), we included an extra column, $m = m_{fail}$, where we tallied the normalized multiplicity distribution of the generated events that failed the acceptance and selection cuts. For fixed (true multiplicity) n, A(n, m) is the distribution of the observed values of m, as illustrated in Fig 3.2.

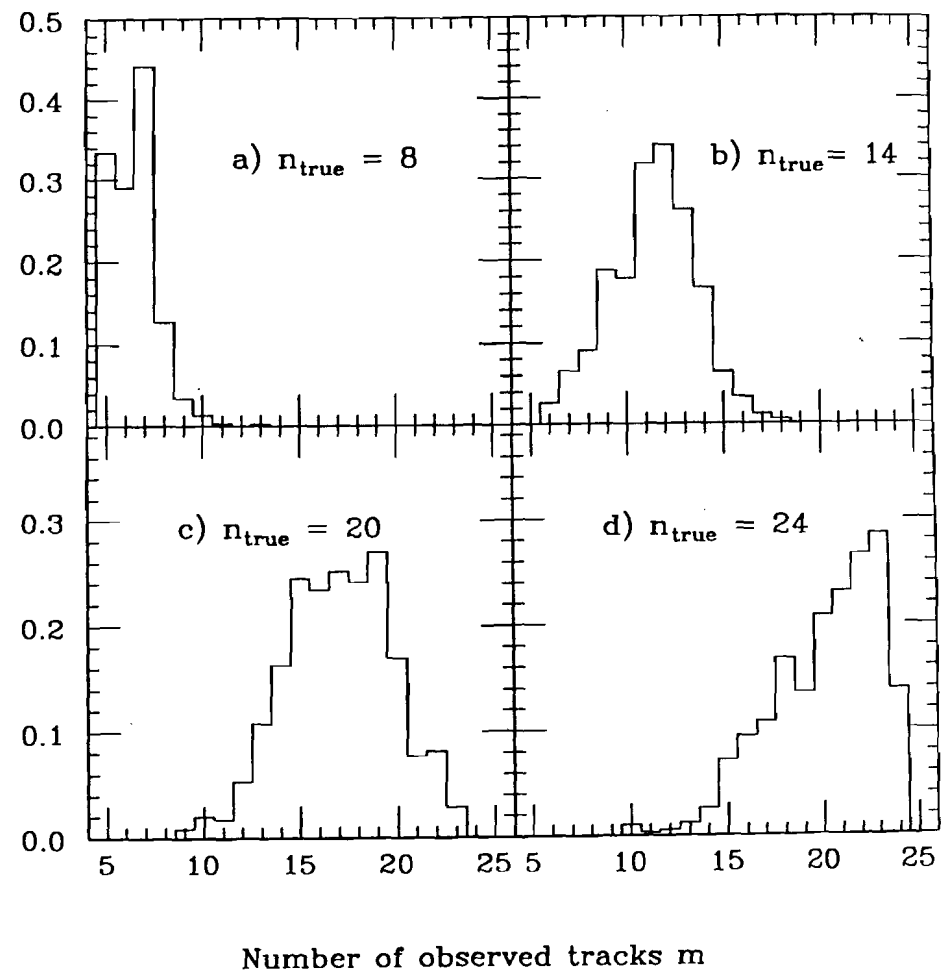

Figure 3.2: The observed multiplicity distributions for generated multiplicities of n = 8 a), 14 b), 20 c), and 24 d), as determined from the 56 GeV Monte Carlo simulated data sample.

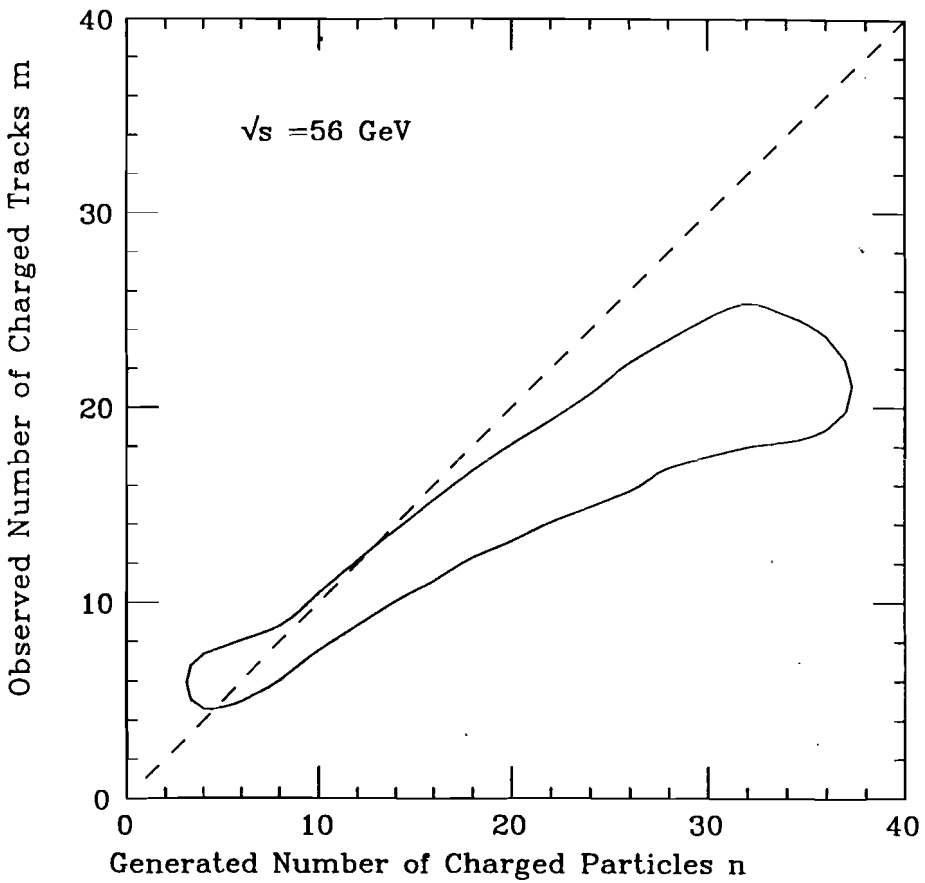

Figure 3.3: The enclosed area indicates the r.m.s. range in values of the observed charged multiplicity m for different values of the generated multiplicity n, as determined from simulated Monte Carlo events. The dashed line corresponds to $m = n$.

The root-mean-squared spread of the observed number of tracks versus the true number of particles is indicated by the closed curve in Fig 3.3. On average, there is a loss of charged particles, but, as can be seen in Fig 3.2 and 3.3, the observed multiplicity is sometimes larger than the true multiplicity. At low multiplicities, the average observed number of tracks is only slightly smaller than the generated number. For high multiplicity events, however, the distortion is substantial. The true multiplicity distribution $N^{MC}_{gen}(n)$ generated by Monte Carlo and the observed multiplicity distribution $N^{MC}_{obs}(m)$ are related by

$$N^{MC}_{gen}(n) = \sum_m A(n,m) \cdot N^{MC}_{obs}(m).$$

The entry $N^{MC}_{obs}(m_{fail})$ is the number of generated events that fail to survive the acceptance and selection criteria.

3.2.3 Correction for Initial State Radiation

The second step corrects for the effects of QED initial-state radiation. We define a correction factor as

$$C(n) = \frac{\rho(n)^{NR}_{gen}}{\rho(n)^{RD}_{gen}},$$

where $\rho(n)^{RD}_{gen}$ and $\rho(n)^{NR}_{gen}$ are the normalized multiplicity distributions for events generated with the QED initial-state radiation turned on and off, respectively. For n values that occur with significant probability, the correction factors are near 1. For example, for n equal to 10, the factor is 0.7, and for n equal to 30, it is 1.4.

We obtained the corrected charged particle multiplicity distribution $N_{cor}(n)$ from

$$N_{cor}(n) = C(n) \cdot \sum_m A(n,m) \cdot N_{obs}(m),$$

where $N_{obs}(m)$ is the observed charged particle multiplicity distribution of final selected experimental data. The entry $N_{obs}(m_{fail})$ was determined from the estimated acceptance and selection efficiency.

Because of the event selection requirement of five or more observed charged tracks, the lowest value of n where $N_{cor}(n)$ is directly derived from the data was $n = 6$. The values of $N_{cor}(n)$ for $n = 2$ and 4 were deduced from the Monte Carlo prediction after normalizing to the data.

3.3 Systematic Errors

We studied seven possible sources of systematic uncertainty in our multiplicity determination. The procedures used to estimate the systematic errors are described below. Table 3.1 summarizes the results.

3.3.1 Selection Efficiency

Since the events that fail our acceptance and selection criteria have a different multiplicity distribution than those that pass (Fig. 3.4), our results depend upon our understanding of the efficiency of these cuts, which is determined from the simulated event sample. By examining how the estimated acceptance changes when different Monte Carlo event generators and different versions of the detector simulation algorithms are used, we determined a 2% uncertainty for this efficiency. A more detailed description of the acceptance calculation and the estimates of its uncertainty is given in reference [27]. Varying the efficiency by this amount results in a 0.3% change in the resulting value of $< n >$, which we have taken as the systematic error caused by this effect.

3.3.2 CDC Smearing

We rely on the detector simulation to determine the track-finding efficiency. To test our sensitivity to the details of the simulation, we increased the CDC smearing parameters by a factor of 1.5, at which point the data and MC start to disagree substantially (see Fig. 3.5), and examined the change in the measured charged multiplicity. We found the variation $\Delta < n > / < n >$ to be less than 1.0% and have used 1% as the systematic error associated with detector smearing.

3.3.3 Initial-state Radiation

QED initial-state radiation reduces the center-of-mass energy of the e^+e^- collision, distorting the multiplicity distribution. The energy spectrum of the initial state radiated photon is shown in Fig. 3.6. There are divergences when the radiated photon energy, E_γ, is zero and when $E_\gamma = E_{beam}$. Events near the $E_\gamma = E_{beam}$ pole have radiated photons that tend to be collinear with the beam and, thus,

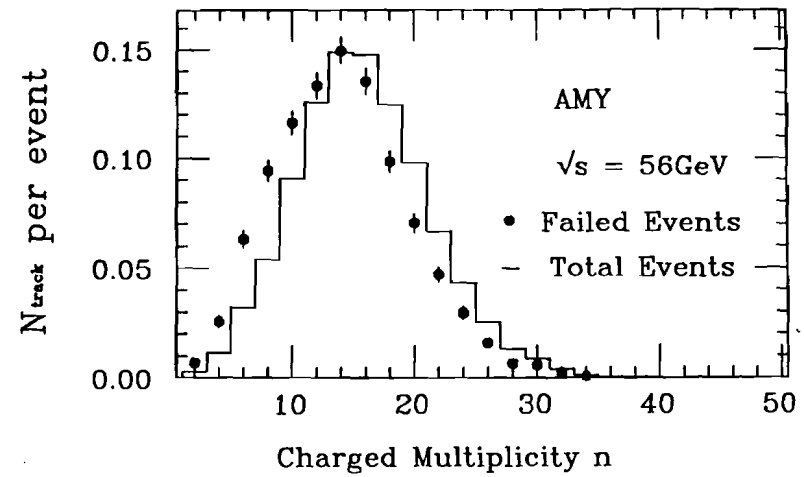

Figure 3.4: The charged multiplicity distribution for the total generated events (histogram) and the generated events which failed our acceptance and selection criteria (points).

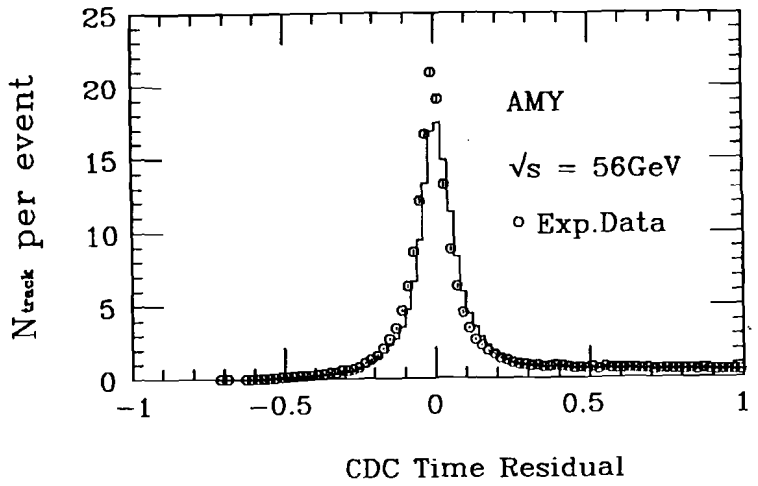

Figure 3.5: The CDC time residual distribution for the experimental data (points) and the MC simulated data with a smearing parameter increased by a factor of 1.5. The poor agreement between data and MC in this figure should be compared with the results for our preferred values of the smearing parameters shown in Fig. 2.7.

these events are usually confined to the beam pipe and not seen in the detector. Figure 3.7 shows the integral distribution of the fraction of the accepted simulated events that have an initial state radiation (i.s.r.) photon with energy between different values of E_γ and $0.99E_{beam}$. Normally, when we compute radiative corrections, we avoid the pole by allowing the energy of the i.s.r. photon to range up to a maximum value of $E_\gamma = 0.99E_{beam}$ and, thus, the radiative correction does not consider those events with $E_\gamma > 0.99E_{beam}$. From the results shown in Fig. 3.7 we estimate that there are less than two events with $E_\gamma > 0.99E_{beam}$ in our data sample and these have a negligible effect on our results.

We correct our data by comparing the results from Monte Carlo event samples with and without initial-state radiation. Upon application of this correction, the average multiplicity $< n >$ increased 8% and the dispersion D decreased 7%. We have estimated that the radiative corrections themselves are done with a precision of approximately 5% [27]. We therefore assign a 0.4% systematic error to the correction of $< n >$.

3.3.4 $\gamma \rightarrow e^+e^-$ Conversion

The average number of tracks that originate from photon conversions was estimated from the Monte Carlo simulation to be 0.29 per event, or $\sim$ 2% of the observed multiplicity. We checked the reliability of the Monte Carlo calculation in two ways. The number of photons with energy greater than 2.5 GeV observed in the SHC was compared with the Monte Carlo predictions (Fig. 2.6 (b)) and agreement was found at the 99% level. Additionally, photons converting in the beam pipe or ITC were reconstructed in the CDC; their measured number agrees with the Monte Carlo calculation at the 97% level. We estimate that the uncertainty in our measurement due to this correction is 0.1%. Nuclear interactions in the beam-pipe and inner material of the detector were modeled using the Monte Carlo program by Grant [38]. Since the interaction probability is one third that for photon conversion, the systematic error associated with nuclear interactions is expected to be negligibly small.

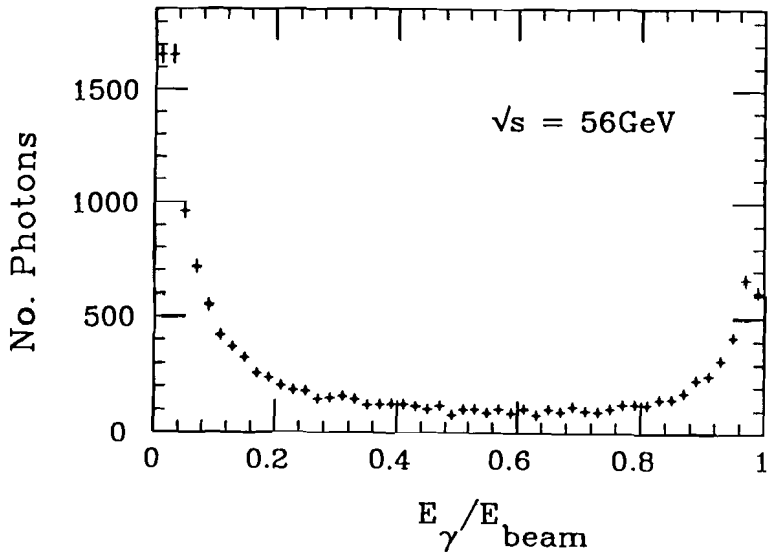

Figure 3.6: The energy spectrum of the initial state radiated photon produced by the Lund 6.3 generator.

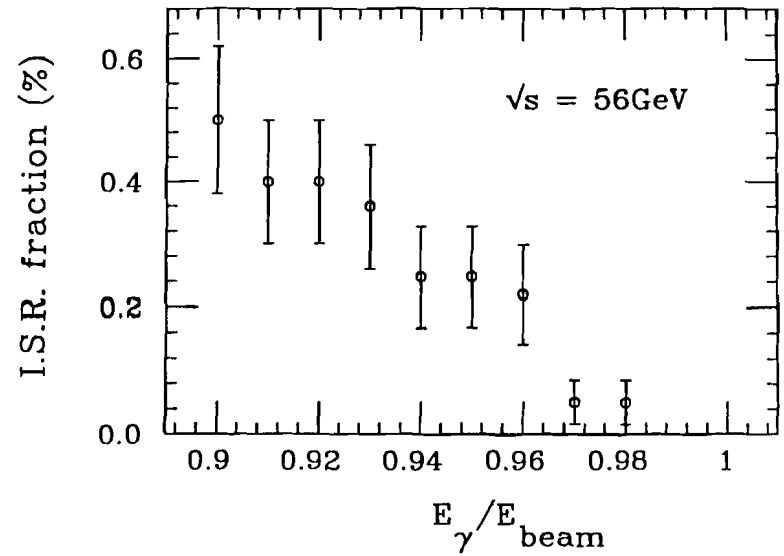

Figure 3.7: The integral distribution of the fraction of accepted MC events that contain initial state radiation photons with energies between E_γ and $0.99E_{beam}$. From this we estimate the fraction of events in the data with photon energy between $0.99E_{beam}$ and E_{beam} to be less than 0.05%.

3.3.5 MC Event Generator

The correction procedure relies on the QCD event generator. We use the Lund 6.3 (parton-shower) event generator because it has been shown to give an accurate description of the general properties of multihadron events in our energy range [36]. To assess the sensitivity of our results to the details of the event generator, we repeated our analysis with the Lund 6.2 (matrix-element with string-fragmentation) generator [28]. This model does not reproduce the observed charged multiplicity very well, as can be seen in Fig 3.1 (b). We have defined a the distribution:

$$T(n) = fN_{6.2}(n) + (1 - f)N_{6.3}(n) \quad ,$$

where f is a parameter very from 0 to 1, and $N_{6.3}(n)$ and $N_{6.2}(n)$ are the observed charged multiplicity distributions expected from the Lund 6.3 (Parton Shower) model and the Lund 6.2 (Matrix Element) model. When $f = 0$ (1), T(n) is same as the distribution of Lund 6.3 (Lund 6.2). If we fit the observed charged multiplicity distribution with $T(n)$ by varying f, we find a minimum χ^2/d.o.f. = 28/21 for $f = 0$. Fig. 3.8 shows the χ^2 distribution as a function of f. We chose the point corresponding to $\Delta\chi^2 = 10$ from χ^2_{min}, corresponding to $f = 0.5$, namely a mixture of equal numbers of events for Lund 6.2 and 6.3 (χ^2/d.o.f. = 2.0), as a reasonably extreme variation of the MC generator for purposes of estimating the associated systematic error. This corresponds to a 2.5% systematic error for $< n >$ and is the dominant systematic error on the individual points of the multiplicity distributions.

3.3.6 Low Multiplicity

Since our event-selection criteria eliminated low-multiplicity events, we must take these results from an extrapolation of the parton-shower model results. As an estimate of the error associated with these points, we take the difference between the modified-Poisson distribution values, which follow the parton-shower model's results in this region fairly closely, and the pair-Poisson distribution values, which are higher than the Monte Carlo, as representative of the range of uncertainty. This gives an estimate of the uncertainty in $< n >$ due to the extrapolation to $n = 2$ and $n = 4$ of 0.6%.

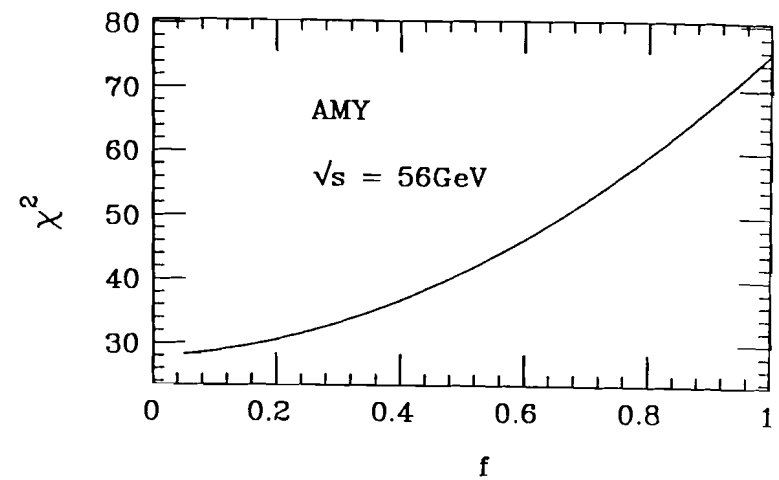

Figure 3.8: The χ^2 distribution as a function of f

systematic errors	(%)
detection efficiency	0.3
track finding efficiency	1.0
initial state radiations	0.4
$\gamma \rightarrow e^+e^-$ conversion	0.1
Monte Carlo scheme	2.5
low multiplicity	0.6
event selection	0.3
overall systematic error	2.8

Table 3.1: Summary of the systematic error of $< n >$.

3.3.7 Event Selection Cut

The multihadron event and track-selection criteria could be another source of systematic error. To estimate the magnitude of this uncertainty we changed the selection criteria and examined the effect on the measured charge multiplicity. For example, repeating the entire analysis with the cut on the angle of the thrust axis changed from $|cos\theta_T| < 0.70$, to $|cos\theta_T| < 0.50$, results in a 0.23% change in the average multiplicity. Similar studies of the effects due to the track and event selection criteria, showed a negligible effect on the measured average multiplicity. We assign a 0.3% systematic error to the effect of the track and event selection.

We have combined the uncertainties from the sources described in quadrature to obtain an estimate of the overall systematic uncertainty of our multiplicity measurement of 2.8%. These errors are summarized in Table 3.1.

3.4 Point-to-point Systematic Error

Since the dominant component of the overall systematic error comes from the choice of MC event generator, it is reasonable to estimate the point-to-point systematic error of the multiplicity distribution by using the difference that results from switching from the Lund 6.3 to the Lund 6.2 Monte Carlo program. Fig. 3.9 shows the charged multiplicity distribution of the $\sqrt{s} = 56$ GeV observed experimental data corrected by the Lund 6.3 (solid circles) and Lund 6.2 (open boxes) correction matrix respectively. We chose half the difference between the two re-

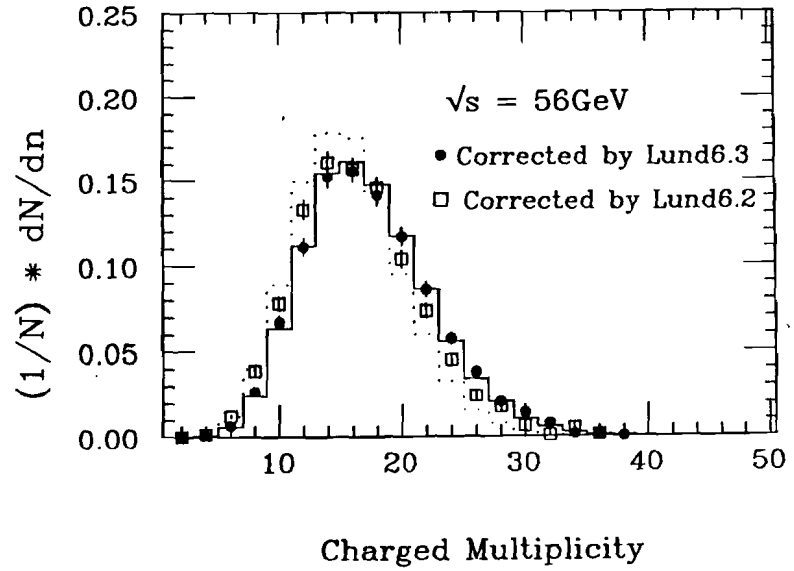

Figure 3.9: The multiplicity distribution of the experiment data at center-of-mass energy equals to 56GeV corrected by Lund 6.3 (solid points) and Lund 6.2 (open boxes) correction matrix, compare with Lund 6.3 MC (solid histogram) and Lund 6.2 (dotted histogram)

sults as an estimate of the point-to-point systematic error. In order to determine these differences, we combined all our data from all energies and corrected using the $\sqrt{s} = 56$ GeV correction matrix. There were large fluctuations in these differences, particularly near $n = 12$ where the multiplicity distribution is changing most rapidly. These were smoothed by forcing the error at each point to agree with the average value of its neighboring points. These point-to-point systematic errors are typically 5% $\sim$ 10%. The relative point-to-point systematic error at each individual energy was taken to be the same as that for the $\sqrt{s} = 56$ GeV data.

Chapter 4

Results

4.1 Charged Multiplicity Distribution

The fully corrected multiplicity distributions for the eight center-of-mass energies in our full data sample are listed in Table 4.1; the results for all energies combined ($< \sqrt{s} >$ = 57 GeV) are given in the final column of the table. For each entry, the first error indicates the statistical uncertainty and the second gives the estimated systematic error. The $n = 2$ and $n = 4$ points were derived using the Lund 6.3 MC normalized to the observations for higher n values; the corresponding errors are systematic only. The multiplicity distribution for all energies combined ($< \sqrt{s} >$=57 GeV) is shown in Fig. 4.1.

There is excellent agreement with the Lund parton-shower model. Neither the modified-Poisson nor the pair-Poisson distributions provide good representations of the data. Summaries of the characteristics of the eight data sets and of the properties of the multiplicity distributions are listed in Table 4.2. Of particular note are the f_2 moments, where $f_2 = D^2 - < n >$. These are statistically significantly non-zero, reflecting the large disagreement between the data points and the modified-Poisson curves in Fig. 4.1.

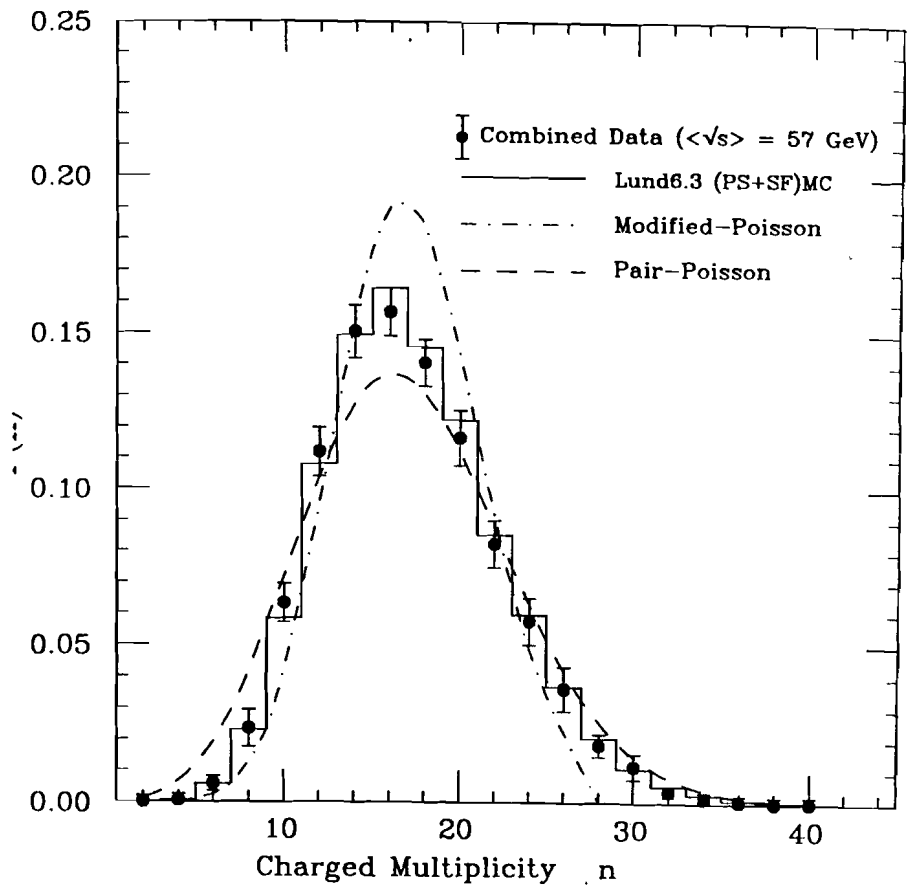

Figure 4.1: The corrected charged multiplicity distribution for all energies combined compared with the predictions of the Lund 6.3 (Parton-Shower and String-Fragmentation) model (solid histogram), the modified-Poisson (dot-dash curve), and pair-Poisson (dashed curve) distributions. The mean center-of-mass energy is 57 GeV.

n	$\sqrt{s} = 50GeV$	$\sqrt{s} = 52GeV$	$\sqrt{s} = 55GeV$
2	0.0127 ± 0.0097	0.0125 ± 0.0094	0.0036 ± 0.0038
4	0.076 ± 0.039	0.074 ± 0.037	0.076 ± 0.035
6	$0.68 \pm 0.17 \pm 0.27$	$0.638 \pm 0.096 \pm 0.256$	$0.72 \pm 0.13 \pm 0.29$
8	$3.35 \pm 0.97 \pm 0.82$	$3.00 \pm 0.42 \pm 0.73$	$2.68 \pm 0.48 \pm 0.65$
10	$7.67 \pm 2.27 \pm 0.64$	$7.39 \pm 0.99 \pm 0.62$	$6.91 \pm 1.15 \pm 0.58$
12	$13.90 \pm 3.94 \pm 0.70$	$12.96 \pm 1.69 \pm 0.65$	$12.40 \pm 1.84 \pm 0.62$
14	$18.13 \pm 4.98 \pm 0.54$	$16.12 \pm 2.07 \pm 0.48$	$16.38 \pm 2.37 \pm 0.49$
16	$16.92 \pm 4.73 \pm 0.12$	$15.56 \pm 2.02 \pm 0.11$	$15.80 \pm 2.35 \pm 0.12$
18	$13.95 \pm 4.25 \pm 0.18$	$14.15 \pm 1.96 \pm 0.18$	$14.04 \pm 2.22 \pm 0.18$
20	$9.98 \pm 3.58 \pm 0.50$	$11.24 \pm 1.80 \pm 0.56$	$12.03 \pm 2.11 \pm 0.60$
22	$6.05 \pm 2.41 \pm 0.39$	$7.14 \pm 1.31 \pm 0.46$	$7.92 \pm 1.58 \pm 0.52$
24	$4.34 \pm 1.96 \pm 0.45$	$5.37 \pm 1.19 \pm 0.56$	$5.03 \pm 1.08 \pm 0.52$
26	$2.41 \pm 1.20 \pm 0.40$	$3.03 \pm 0.85 \pm 0.50$	$3.06 \pm 0.80 \pm 0.50$
28	$1.37 \pm 0.66 \pm 0.22$	$1.69 \pm 0.47 \pm 0.28$	$1.41 \pm 0.39 \pm 0.23$
30	$0.84 \pm 0.43 \pm 0.28$	$1.19 \pm 0.46 \pm 0.39$	$0.86 \pm 0.30 \pm 0.28$
32	$0.18 \pm 0.12 \pm 0.08$	$0.27 \pm 0.11 \pm 0.12$	$0.29 \pm 0.14 \pm 0.13$
34	$0.09 \pm 0.05 \pm 0.01$	$0.11 \pm 0.06 \pm 0.02$	$0.33 \pm 0.27 \pm 0.05$
36	$0.04 \pm 0.03 \pm 0.07$	$0.04 \pm 0.02 \pm 0.06$	$0.04 \pm 0.03 \pm 0.07$
38	$0.02 \pm 0.02 \pm 0.03$	$0.03 \pm 0.02 \pm 0.06$	$0.02 \pm 0.02 \pm 0.04$

Table 4.1: The charged multiplicity distributions $1/N_{ev}$ (dN/dn) in percent. The final column lists the results from all energies combined (average center-of-mass energy equals to 57 GeV). Statistical errors are listed first and systematic errors second. For the $n = 2$ and $n = 4$ points only systematic errors are given.

n	$\sqrt{s} = 56GeV$	$\sqrt{s} = 57GeV$	$\sqrt{s} = 60GeV$
2	0.0058 ± 0.0061	0.0025 ± 0.0026	0.0082 ± 0.0085
4	0.069 ± 0.033	0.065 ± 0.031	0.071 ± 0.036
6	$0.66 \pm 0.08 \pm 0.26$	$0.72 \pm 0.11 \pm 0.29$	$0.49 \pm 0.09 \pm 0.20$
8	$2.61 \pm 0.28 \pm 0.64$	$2.58 \pm 0.37 \pm 0.63$	$2.00 \pm 0.34 \pm 0.49$
10	$6.67 \pm 0.74 \pm 0.56$	$6.11 \pm 0.81 \pm 0.51$	$5.77 \pm 0.88 \pm 0.48$
12	$11.04 \pm 1.18 \pm 0.55$	$10.15 \pm 1.36 \pm 0.51$	$11.01 \pm 1.59 \pm 0.55$
14	$15.17 \pm 1.52 \pm 0.45$	$14.33 \pm 1.81 \pm 0.42$	$13.24 \pm 1.89 \pm 0.39$
16	$15.54 \pm 1.58 \pm 0.11$	$15.04 \pm 1.93 \pm 0.11$	$15.27 \pm 2.21 \pm 0.11$
18	$14.08 \pm 1.58 \pm 0.18$	$14.82 \pm 1.96 \pm 0.19$	$13.89 \pm 2.11 \pm 0.17$
20	$11.66 \pm 1.46 \pm 0.58$	$12.75 \pm 1.88 \pm 0.64$	$11.33 \pm 1.89 \pm 0.57$
22	$8.55 \pm 1.20 \pm 0.56$	$9.09 \pm 1.54 \pm 0.59$	$10.00 \pm 1.87 \pm 0.65$
24	$5.71 \pm 0.93 \pm 0.59$	$5.95 \pm 1.21 \pm 0.62$	$6.48 \pm 1.40 \pm 0.67$
26	$3.76 \pm 0.76 \pm 0.62$	$4.09 \pm 1.00 \pm 0.68$	$4.91 \pm 1.22 \pm 0.81$
28	$2.06 \pm 0.46 \pm 0.34$	$1.88 \pm 0.53 \pm 0.31$	$2.53 \pm 0.84 \pm 0.41$
30	$1.38 \pm 0.35 \pm 0.45$	$1.33 \pm 0.51 \pm 0.43$	$1.20 \pm 0.41 \pm 0.39$
32	$0.76 \pm 0.22 \pm 0.34$	$0.72 \pm 0.27 \pm 0.33$	$0.93 \pm 0.48 \pm 0.42$
34	$0.14 \pm 0.06 \pm 0.02$	$0.25 \pm 0.13 \pm 0.04$	$0.46 \pm 0.23 \pm 0.07$
36	$0.10 \pm 0.04 \pm 0.19$	$0.05 \pm 0.03 \pm 0.10$	$0.26 \pm 0.24 \pm 0.48$
38	$0.01 \pm 0.01 \pm 0.02$	$0.08 \pm 0.04 \pm 0.14$	$0.13 \pm 0.10 \pm 0.23$
40			$0.01 \pm 0.01 \pm 0.02$

Table 4.1: (Continued)

n	$\sqrt{s} = 60.8GeV$	$\sqrt{s} = 61.4GeV$	$< \sqrt{s} >= 57GeV$ (combined data)
2	0.0024 ± 0.0025	0.0023 ± 0.0025	0.0032 ± 0.0014
4	0.041 ± 0.018	0.040 ± 0.018	0.050 ± 0.020
6	$0.51 \pm 0.09 \pm 0.21$	$0.49 \pm 0.08 \pm 0.20$	$0.59 \pm 0.03 \pm 0.24$
8	$2.06 \pm 0.34 \pm 0.50$	$1.94 \pm 0.29 \pm 0.47$	$2.35 \pm 0.13 \pm 0.58$
10	$5.76 \pm 0.93 \pm 0.48$	$5.84 \pm 0.85 \pm 0.49$	$6.33 \pm 0.33 \pm 0.53$
12	$10.36 \pm 1.59 \pm 0.52$	$10.98 \pm 1.51 \pm 0.55$	$11.19 \pm 0.56 \pm 0.56$
14	$14.77 \pm 2.11 \pm 0.44$	$15.42 \pm 1.99 \pm 0.46$	$15.03 \pm 0.72 \pm 0.45$
16	$16.30 \pm 2.38 \pm 0.12$	$16.29 \pm 2.17 \pm 0.12$	$15.66 \pm 0.76 \pm 0.11$
18	$13.88 \pm 2.14 \pm 0.17$	$13.39 \pm 1.91 \pm 0.17$	$14.04 \pm 0.73 \pm 0.18$
20	$11.81 \pm 1.90 \pm 0.59$	$11.30 \pm 1.69 \pm 0.57$	$11.64 \pm 0.66 \pm 0.58$
22	$8.50 \pm 1.64 \pm 0.55$	$8.11 \pm 1.45 \pm 0.53$	$8.23 \pm 0.54 \pm 0.54$
24	$6.68 \pm 1.47 \pm 0.69$	$6.42 \pm 1.33 \pm 0.66$	$5.75 \pm 0.44 \pm 0.60$
26	$4.21 \pm 1.17 \pm 0.70$	$4.26 \pm 1.09 \pm 0.71$	$3.61 \pm 0.34 \pm 0.60$
28	$2.37 \pm 0.70 \pm 0.39$	$2.53 \pm 0.73 \pm 0.41$	$1.84 \pm 0.19 \pm 0.30$
30	$1.24 \pm 0.41 \pm 0.40$	$1.43 \pm 0.47 \pm 0.47$	$1.15 \pm 0.14 \pm 0.38$
32	$0.76 \pm 0.28 \pm 0.35$	$0.81 \pm 0.28 \pm 0.37$	$0.37 \pm 0.06 \pm 0.17$
34	$0.46 \pm 0.20 \pm 0.07$	$0.42 \pm 0.16 \pm 0.06$	$0.14 \pm 0.03 \pm 0.02$
36	$0.24 \pm 0.14 \pm 0.44$	$0.20 \pm 0.10 \pm 0.36$	$0.05 \pm 0.01 \pm 0.09$
38	$0.01 \pm 0.01 \pm 0.01$	$0.02 \pm 0.01 \pm 0.03$	$0.01 \pm 0.01 \pm 0.09$
40	$0.05 \pm 0.02 \pm 0.09$	$0.10 \pm 0.05 \pm 0.18$	$0.01 \pm 0.01 \pm 0.09$

Table 4.1: (Continued)

$\sqrt{s}$	50 GeV	52 GeV	55 GeV	56 GeV
No.events	77	396	288	604
L (pb^{-1})	0.64 ± 0.02	3.98 ± 0.04	3.27 ± 0.04	5.99 ± 0.05
$< n >$	16.24 ± 0.41	16.74 ± 0.19	16.82 ± 0.22	17.27 ± 0.16
D	4.78 ± 0.28	5.00 ± 0.17	4.95 ± 0.17	5.20 ± 0.13
f_2	6.66 ± 2.71	8.32 ± 1.66	7.66 ± 1.73	9.80 ± 1.37
$< n > /D$	3.40 ± 0.22	3.35 ± 0.12	3.40 ± 0.13	3.32 ± 0.08
K GD fit	11.9 ± 0.8	11.7 ± 0.6	11.6 ± 0.8	13.3 ± 0.4
χ^2/d.o.f.	5/18	8/18	6/18	23/18
k NB fit	71.0 ± 2.5	47.7 ± 7.4	56.5 ± 8.8	46.7 ± 5.6
χ^2/d.o.f.	6/18	8/18	5/18	9/18

Table 4.2: Summaries of the multiplicity distributions at each energy.

$\sqrt{s}$	57 GeV	60 GeV	60.8 GeV	61.4 GeV
No.events	393	320	299	363
L (pb^{-1})	4.40 ± 0.05	3.55 ± 0.04	3.49 ± 0.05	4.33 ± 0.05
$< n >$	17.49 ± 0.19	17.85 ± 0.23	17.66 ± 0.23	17.61 ± 0.21
D	5.19 ± 0.17	5.43 ± 0.21	5.29 ± 0.18	5.35 ± 0.17
f_2	9.54 ± 1.73	11.63 ± 2.26	10.41 ± 1.93	11.09 ± 1.87
$< n > /D$	3.37 ± 0.11	3.29 ± 0.13	3.34 ± 0.12	3.29 ± 0.11
K GD fit	11.1 ± 0.7	13.2 ± 0.4	14.8 ± 0.3	13.1 ± 0.4
χ^2/d.o.f.	7/18	19/19	32/19	23/19
k NB fit	46.2 ± 6.2	40.1 ± 4.7	63.8 ± 8.9	55.4 ± 7.4
χ^2/d.o.f.	8/18	7/19	16/19	18/19

Table 4.2: (Continued)

$\sqrt{s}$	$<\sqrt{s}>$=57 GeV
No. events	2740
L (pb^{-1})	29.6
< n >	$17.19 \pm 0.07 \pm 0.48$
D	$5.03 \pm 0.06 \pm 0.25$
f_2	8.11 ± 0.59
< n > /D	3.42 ± 0.04
K GD fit	12.0 ± 0.4
χ^2/d.o.f.	18/19
k NB fit	52.8 ± 4.3
χ^2/d.o.f.	21/19

Table 4.2: (Continued)

4.2 Energy Dependence of The Charged Multiplicity

Fig. 4.2 shows the dependence of < n > on the center-of-mass energy for this experiment and for other e^+e^- experiments, including recent results at $\sqrt{s}$ = 91 GeV [12, 13, 44, 45].

The variation of $< n >$ with $\sqrt{s}$, for all of the data shown in Fig. 4.2, were fitted with the following functions:

1. Fitting to the form derived from the fireball and hydrodynamical models for hadron-hadron interactions, [46]

$$< n >= a \cdot s^b,$$

yields $a = 2.20 \pm 0.03$ and $b = 0.252 \pm 0.002$ with $\chi^2 = 143$ for 86 degrees of freedom (d.o.f.). Note that the fitted value for the exponent b is consistent with the $s^{1/4}$ behaviour first predicted by Fermi [3]. The results of this fit are shown in Fig. 4.2 as a solid curve.

2. Fitting to the empirical relationship from analyses of pp data [7]

$$< n >= a + b \cdot \ln s + c \cdot \ln^2 s,$$

yields $a = 3.37 \pm 0.09$, b = -0.43 $\pm$0.06, and $c = 0.262 \pm 0.007$ with χ^2 = 93 for 85 d.o.f. This fit is shown as a dashed curve in Fig. 4.2.

3. Fitting to the form suggested by leading logarithm QCD [4, 5, 6],

$$< n >= a + b \cdot \exp\left[c\sqrt{\ln(s/Q_0^2)}\right],$$

with c taken to be 1.769, gives $a = 2.46 \pm 0.02$, $b = 0.091 \pm 0.001$, and $Q_0^2 = 0.85 \pm 0.02$ GeV^2, with $\chi^2 = 88$ for 85 d.o.f. The fit is shown as a dot-dash curve in Fig. 4.2.

In fact, the above curves are not expected to be precise representations of the charged multiplicity at lower energies where resonances and thresholds are expected to produce small-scale fluctuations. If we limit the fits to center-of-mass energies above 5 GeV, well above the threshold for charmed particle production, the three

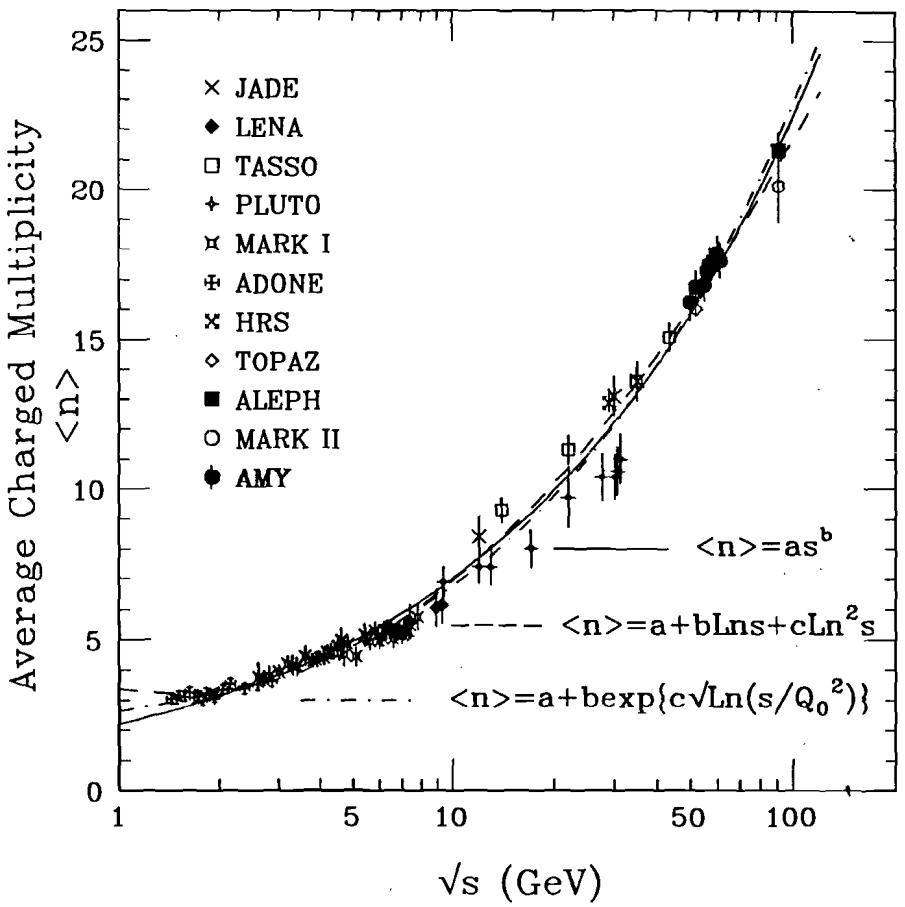

Figure 4.2: The average charged multiplicity in e^+e^- annihilation as a function of center-of-mass energy, including results from other experiments. The curves show the fits to the data (see text).

cases give fits of similar quality ($\chi^2/d.o.f.$ = 69/50, 60/49, and 61/49 for cases 1, 2, and 3, respectively). All of the above functions describe the high energy data equally well; differences between them only become significant at center-of-mass energies above 100 GeV.

Fig. 4.3 (a) shows the dispersion D as a function of $\sqrt{s}$. The error bars shown are statistical only; the systematic uncertainties are about 5.0% of the D values. The D values measured in lower energy experiments are also shown in the figure.

The ratio $< n > /D$ is shown as a function of energy in Fig. 4.3 (b), both for this experiment and for previous experiments. This shows some weak energy dependence, increasing slightly with increasing $\sqrt{s}$. The solid (dashed) curve in Fig. 4.3 (b) shows the expectations for a modified-Poisson (pair-Poisson) behaviour of the multiplicity distribution; both cases clearly differ from the measured points.

We fit the results for $< n > /D$ shown in Fig. 4.3 (b) to a single constant value. The fit quality was very poor; $\chi^2/d.o.f.$ = 107. If we restrict the fit to the higher energy points only, the fit quality improves. Fig. 4.4 shows how the value of $\chi^2/d.o.f.$ varies as the lower energy cut-off is increased. The fit quality is good for energies above $\sqrt{s} \sim 20$ *GeV*, where $< n > /D = 3.28 \pm 0.01$. KNO scaling predicts that the ratio $< n > /D$ is independent of $\sqrt{s}$, in agreement with our results for $\sqrt{s} > 20$ GeV.

4.3 KNO Scaling

In Fig. 4.5 we present the KNO distribution for all of our data combined ($< \sqrt{s} >$=57 GeV) together with the 29 GeV data from the HRS experiment [12] and the 34.8 GeV data from the TASSO experiment [13]. There is no marked change in the KNO distribution over the center-of-mass range from 29 to 57 GeV. Fitting the data from the three experiments to a Gamma distribution (GD) (Eq. 1.7) gives values of K of

$$K = 12.0 \pm 0.4 \quad (\chi^2 = 18/19 d.o.f.) \quad AMY\ (57\ GeV)$$

$$K = 10.9 \pm 0.1 \quad (\chi^2 = 71/17 d.o.f.) \quad TASSO\ (34.8\ GeV)$$

$$K = 12.3 \pm 0.3 \quad (\chi^2 = 41/13 d.o.f.) \quad HRS\ (29.0\ GeV)$$

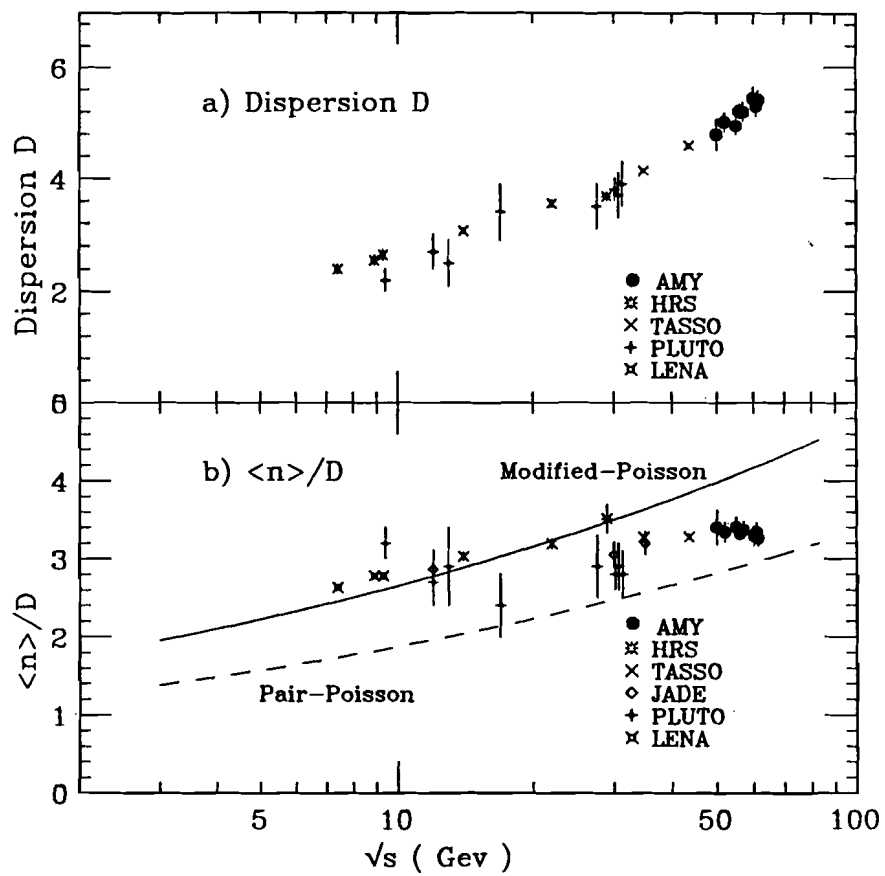

Figure 4.3: (a) The energy dependence of the dispersion D. (b) The energy dependence of $< n > /D$. The dashed curve is the expectation for a pair-Poisson behaviour, the solid curve is that for a modified-Poisson.

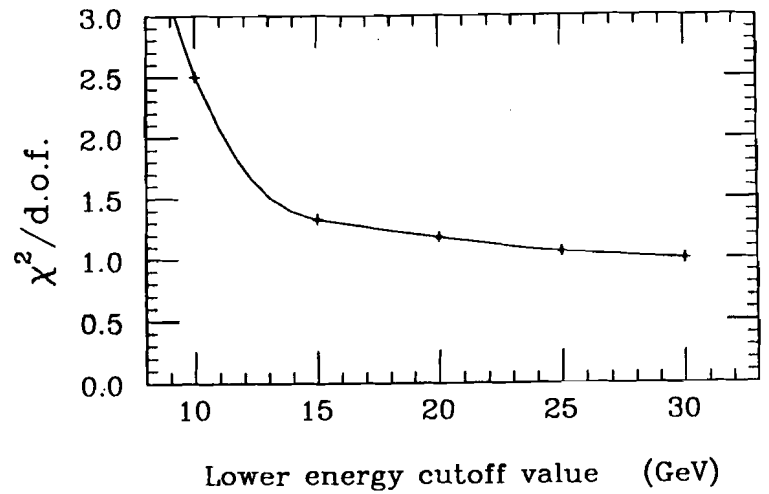

Figure 4.4: Fit quality for $< n > /D$ = constant for different values of the lower energy cut-off.

While the GD shape provides poor fits for the HRS and TASSO data, it fits our data reasonably well. We have fitted the same data to a negative binomial (NB) distribution (Eq. 1.8). The results of these fits are

$$k = 52.8 \pm 4.3 \quad (\chi^2 = 21/19 d.o.f.) \quad AMY\ (57\ GeV)$$

$$k = 54.1 \pm 3.1 \quad (\chi^2 = 39/17 d.o.f.) \quad TASSO\ (34.8\ GeV)$$

$$k = 233.5.0 \pm 53.2 \quad (\chi^2 = 7/13 d.o.f.) \quad HRS\ (29.0\ GeV),$$

and are shown as solid, dotted and dashed curves in Fig. 4.6, respectively. Note that the NB distribution depends both on k and $< n >$, so although the values of k derived from our data and from the HRS results differ, the actual curves agree quite well, leading us to conclude that KNO scaling works well over this energy range. Results for GD and NB fits to the distributions at each of the eight center-of-mass energies and for all the energies combined are given in Table 4.2.

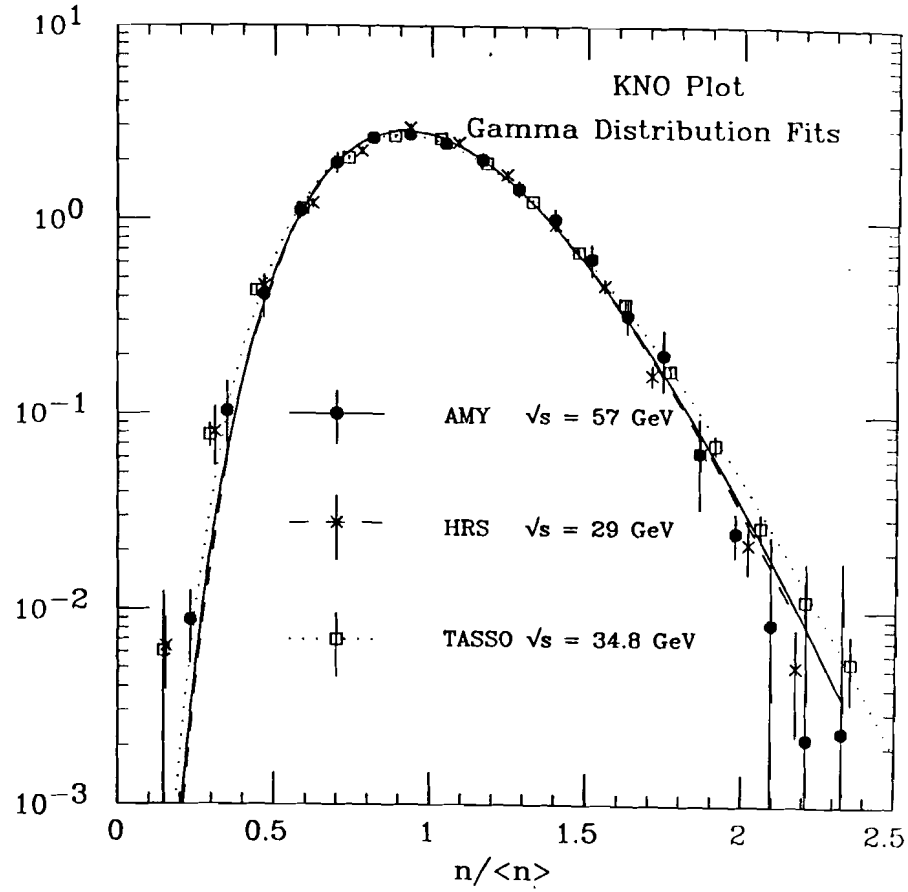

Figure 4.5: The KNO charged multiplicity distribution for the combined data of this experiment compared with measurements at lower energies and with the fitted Gamma distributions.

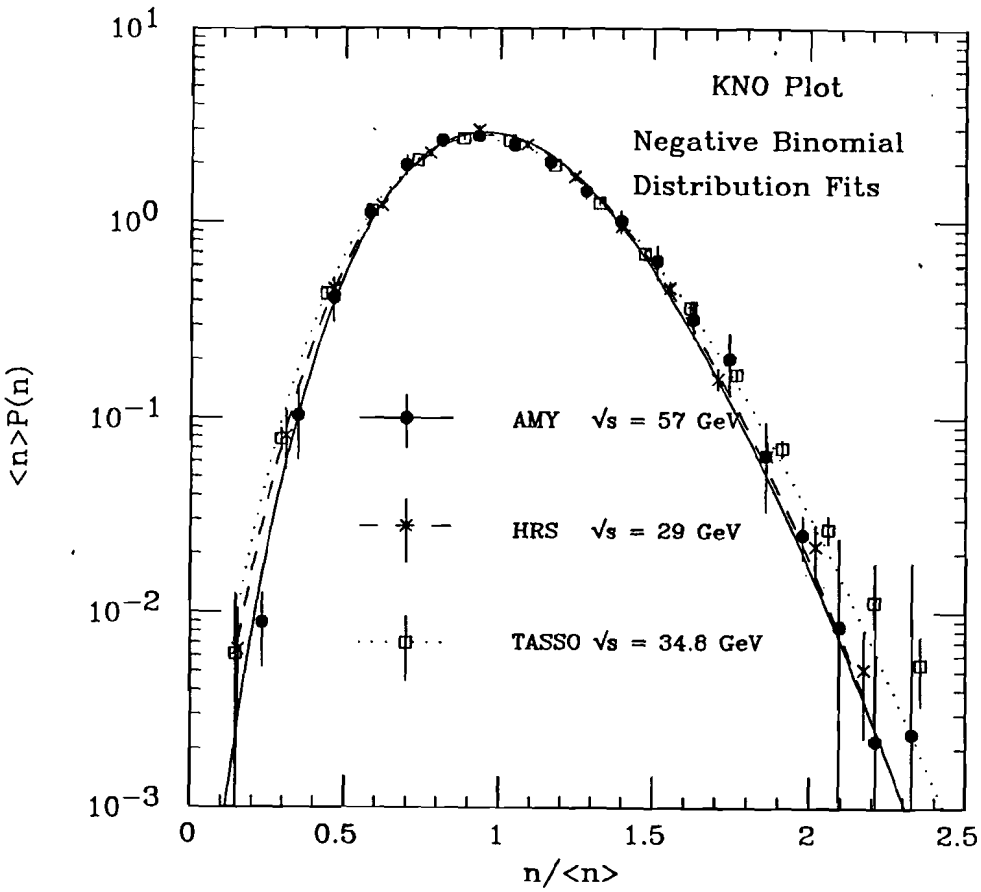

Figure 4.6: The KNO charged multiplicity distribution for the combined data of this experiment compared with measurements at lower energies and with the fitted negative binomial distributions.

Chapter 5

Conclusion

We have presented the multiplicity distributions for charged particles produced in electron positron annihilation at center-of-mass energies ranging from 50 to 61.4 GeV. The charged particle multiplicity distributions are well reproduced by the Lund 6.3 parton-shower model and not by the Lund 6.2 matrix element model.

The average charged particle multiplicity $< n >$ is found to rise with center-of-mass energy and is fitted equally well by Fermi's prediction $< n >= a \cdot s^{1/4}$, the empirical relation $< n >= a + b \cdot \ln s + c \cdot \ln^2 s$, and the QCD motivated form $< n >= a + b \cdot \exp\left[c\sqrt{\ln(s/Q_0^2)}\right]$. The multiplicity distributions are found to deviate significantly from the modified-Poisson distribution at TRISTAN energies. While experiments at lower energy ($\sqrt{s}$ = 29 GeV) show good agreement with a modified-Poisson distribution [12], our results confirm the trend toward distributions that are wider than Poisson-like distributions that were first observed at $\sqrt{s} \geq 34.8$ GeV [13]. The distributions follow KNO scaling; both the Gamma and the negative-binomial distribution functions fit our measured KNO distributions well.

Appendix A

The Central Drift Chamber of the AMY Detector

In this appendix we give a description of the mechanical aspects AMY central drift chamber (CDC), including details of the design and construction. The author was primarily responsible for the construction of this device.

The shell of the CDC is a cylinder of radius 78.7 cm with reentrant endplates as illustrated in Fig. A.1 The spacing of the endplates is maintained at the inner radius by a 1 mm thick KEVLAR tube and at the outer radius by six aluminum posts. Each endplate is a compound structure consisting of six annular rings and five hoops which displace the rings axially to form a reentrant cone-like surface. The rings and hoops are aluminum, and the rings are joined to the hoops using stainless steel screws and structural epoxy (3M 2216). The epoxy forms the gas seal at these seams as well as providing mechanical strength. The apertures between the posts at the outer radius of the chamber are closed structurally by six panels molded to conform to the circumference of the cylinder. The panels are composites of mylar, aluminized mylar, and ROHACELL foam. The panels support a single complete turn of 150 μm thick mylar sheet which forms the gas seal at this surface.

The sense and field wires, which define the 9048 drift cells of the CDC, are secured in holes in opposing rings of the endplates. The 3.4 mm diameter holes were drilled in tandem in the pairs of rings prior to assembly of the endplates. The numerically controlled drilling machine used for this operation placed the holes with a precision of 12 μm (rms). Each hole is fitted with a custom bushing [47] consisting of a brass tube glued with epoxy to a surrounding Delrin sleeve as shown in Fig. A.2. The 20 μm diameter gold-plated tungsten sense wires were bonded

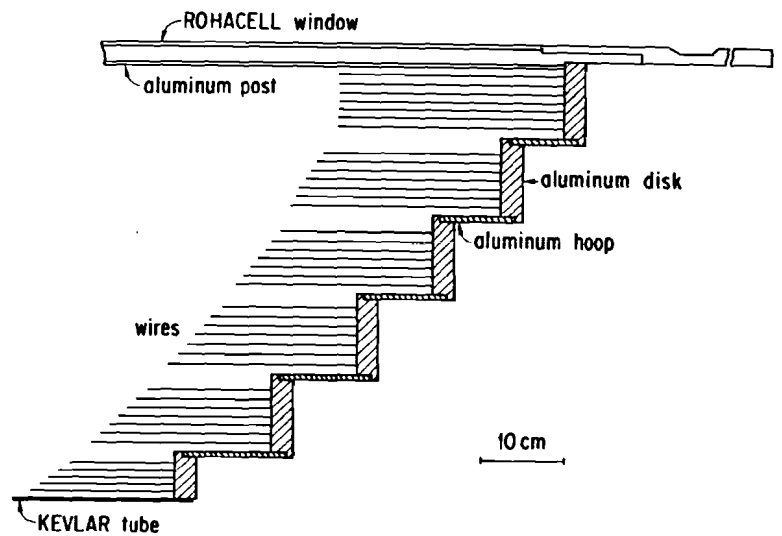

Figure A.1: The endplate of the AMY central drift chamber.

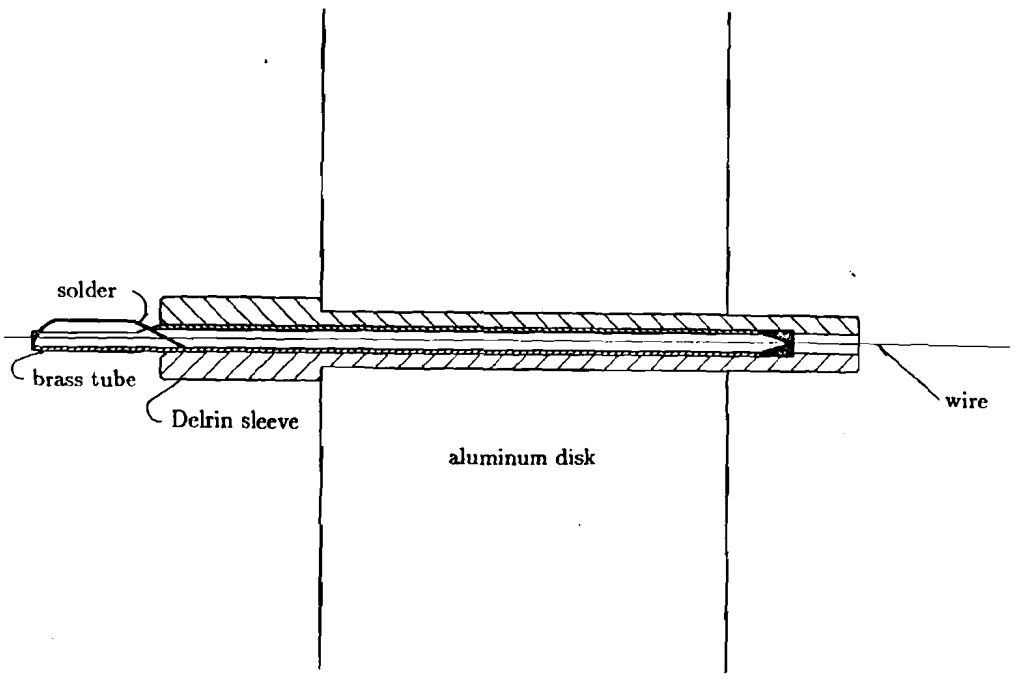

Figure A.2: The wire holding mechanism at the CDC endplate.

to the brass of the bushings using Sn96 solder. The 160 μm diameter gold plated aluminum field wires were bonded to the bushings using KR18 solder, a special solder for aluminum produced by Nihon Almit Co., Tokyo Japan. Adhesion to the solder is the exclusive means of immobilizing the ends of the wires. The solder also seals the aperture in the bushing and provides the electrical connection to the wire. In the fourty months since stringing the wires, four sense wires have slipped from their moorings at one end, and were pulled from the chamber without difficulty. No casualties have occurred among the field wires.

The assembly of the rings and the hoops into a single endplate was done under

a microscope on a three-dimensional measuring table. The relative ring-to-ring precision of the assembly is 20 μm. The two endplates were aligned relative to each other using two opposed theodolites aligned along the axis of the CDC. The endplates were then fixed to the inner KEVLAR tube with epoxy. The precision of the relative endplate alignment is 30 μm. The endplate were prestressed using steel rods to simulate the tension that the wires would ultimately produce. With the steel rods in place we glued the inner carbon fiber tube to the endplates. We removed the rods, and the tension shifted to the tube. As we inserted sense and field wires the tension shifted from the tube to the wires, and at the completion of string the carbon fiber tube was almost stress-free.

The hexagonal geometry of the drift cells is illustrated in Fig. A.3. Since each layer of cells conforms to a cylinder, the hexagons are not precisely regular, and the cell dimensions increase slightly from the innermost to the outermost layer in each band of close-packed layers. Ring 1 supports a single band of five axial layers. Each of rings 2 through 6 supports a band of three small angle stereo layers on the inner portion and a band of four axial layers on the outer portion. The magnitude of the stereo angle is approximately 4.7°, and it varies slightly from ring to ring. The sign also varies in such a way as to minimize the torque on the endplates. In Table A.1 we give several particulars concerning the the geometrical arrangement of the wires.

To make electrical connections to the bushings, we fabricated printed circuit boards with plated-through holes in a pattern exactly matching the positions of a set of bushings. In the plated-through holes we soldered commercially produced "mini-spring sockets" (AMP Corp., part number 1-50871-8) which slide over the exposed brass portion of the bushings. Each circuit board carries 40 to 80 of these connectors. The circuit boards stack on the bushings in two tiers. The lower tier interconnects all of the field wires. The upper tier multilayer circuit boards a) import ground potential to about 30% of the field wires, b) distribute positive high voltage through 10 kΩ resistors to the sense wires, one voltage per layer, c) route the signals via 300 pF high voltage blocking capacitors and a miniature connector to the preamplifiers modules, and d) distribute a calibration pulse delivered via

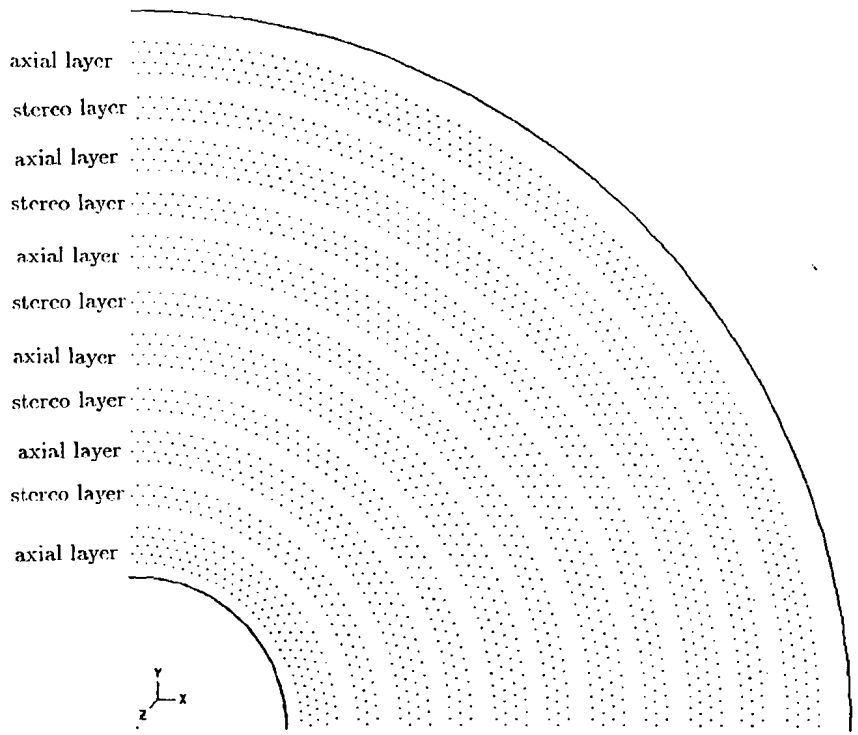

Figure A.3: A quarter of the CDC endplate.

Band Number	Endplate Spacing(cm)	Cylinder Number	Radius (cm)	Stereo Angle	Number of Cells
1	92.4	1	15.50	0	112
		2	16.27	0	112
		3	17.08	0	112
		4	17.93	0	112
		5	18.83	0	112
2	114.4	6	21.24	−4.14°	128
		7	22.16	−4.32°	128
		8	23.12	−4.51°	128
		9	24.87	0	152
		10	25.78	0	152
		11	26.72	0	152
		12	27.69	0	152
3	133.4	13	30.18	4.60°	176
		14	31.12	4.74°	176
		15	32.10	4.88°	176
		16	33.88	0	200
		17	34.81	0	200
		18	35.77	0	200
		19	36.76	0	200
4	150.2	20	39.24	4.83°	232
		21	40.17	4.95°	232
		22	41.12	5.06°	232
		23	42.89	0	248
		24	43.85	0	248
		25	44.82	0	248
		26	45.81	0	248
5	165.2	27	48.31	4.49°	280
		28	49.26	4.58°	280
		29	50.22	4.67°	280
		30	51.99	0	304
		31	52.93	0	304
		32	53.89	0	304
		33	54.86	0	304
6	179.2	34	57.35	−4.89°	328
		35	58.31	−4.97°	328
		36	59.29	−5.06°	328
		37	61.06	0	360
		38	61.99	0	360
		39	62.93	0	360
		40	63.89	0	360

Table A.1: The drift chamber configuration

the high voltage bus to the preamplifier inputs. The preamplifiers dissipate about 700 Watts of heat in a confined space at each end of the CDC. Some of this heat is removed by room temperature air that is circulated through these spaces. In addition, cool water flowing through copper tubes, which are thermally coupled to the endplates, prevents overheating of the endplates themselves.

In order to maintain good transparency for low energy X-rays, we generally employed low-mass, low-Z materials. For example the field wire material is aluminum, and the exit window are thin foam. The material of the chamber is summarized in Table A.2.

The performance of the chamber is described in detail in ref.[20].

Component	Density (gm/cm^3)	Rad. length	Att. length of 10 kV X − ray	Rad. length (%)	Att. of 10 kV X − ray(%)
Kevlar inner tube 1 mm	2.0	42.7 gm/cm^2	.16cm	.47	62.5
Sense wire 20 μm	19.3	.35 cm	4.5 μm	.36	283.
Field wire 160 μm	2.7	8.9 cm	.14 mm	.11	72.6
HRS gas [1]	1.789×10^{-3}	20.65 gm/cm^2	9.68 cm	.45	269. *
Ne-Ethene [2]	1.13×10^{-3}	37.25 gm/cm^2	154. cm	.16	17. *
Rohacell 31 4 mm + glue	.06	42.7 gm/cm^2	6.0 cm	.06	8.
Aluminized Mylar	[3] 1.39 [4] 2.7	42.7 gm/cm^2 8.9 cm	.24 cm .14 mm	.01 .00	1.3 .6
Mylar 150 μm	1.39	42.7 gm/cm^2	.24 cm	.05	6.3

* X-ray is assumed to be emitted at the middle of the CDC.
1) The gas which had been used before installation of the X-ray detector. $Ar/CO_2/CH_4$:89/10/1
2) The gas presently used in the CDC.
3) 32 μm Mylar.
4) 1 μm Al.

Table A.2: Properties of materials used in the CDC.

Appendix B

List of the AMY Collaborators

H.W. Zheng,[a] P. Perez,[a] P. Auchincloss,[a] D. Blanis,[a] A. Bodek,[a] H. Budd,[a] S. Eno,[a] C.A. Fry,[a,h] H. Harada,[a] Y.H. Ho,[a] Y.K. Kim,[a] T. Kumita,[a] T. Mori,[a] S.L. Olsen,[a,i] N.M. Shaw,[a] A. Sill,[a] E.H. Thorndike,[a] K. Ueno,[a] R. Imlay,[b] P. Kirk,[b] J. Lim,[b] R.R. McNeil,[b] W. Metcalf,[b] S.S. Myung,[b] C.P. Cheng,[c] P. Gu,[c] J. Li,[c] Y.K. Li,[c,e] M.H. Ye,[c] Y.C. Zhu,[c] A. Abashian,[d] K. Gotow,[d] K.P. Hu,[d] E.H. Low,[d] M.E. Mattson,[d] L. Piilonen,[d] K.L. Sterner,[d] S. Lusin,[e] C. Rosenfeld,[e] A.T.M. Wang,[e] S. Wilson,[e] M. Frautschi,[f] H. Kagan,[f] R. Kass,[f] C.G. Trahern,[f] R.E. Breedon,[g,h] G.N. Kim,[g,h] Winston Ko,[g] R.L. Lander,[g] K. Maeshima,[g] R.L. Malchow,[g] J.R. Smith,[g] D. Stuart,[g] K. Abe,[h] Y. Fujii,[h] Y. Higashi,[h] S.K. Kim,[h] Y. Kurihara,[h] A. Maki,[h] T. Nozaki,[h] T. Omori,[h] H. Sagawa,[h] Y. Sakai,[h] Y. Sugimoto,[h] Y. Takaiwa,[h] S. Terada,[h] R. Walker,[h,a] F. Kajino,[j] D. Perticone,[k] R. Poling,[k] T. Thomas,[k] Y. Ishi,[l] K. Miyano,[l] H. Miyata,[l] T. Sasaki,[l] Y. Yamashita,[m] A. Bacala,[n,o] J. Liu,[n] I.H. Park,[n] F. Sannes,[n] S. Schnetzer,[n] R. Stone,[n] J. Vinson,[n] S. Kobayashi,[p] A. Murakami,[p] J.S. Kang,[q] H.J. Kim,[q] M.H. Lee,[q] D.H. Han,[r] E.J. Kim,[r] D. Son,[r] T. Kojima,[s] S. Matsumoto,[s] R. Tanaka,[s] Y. Yamagishi,[s] T. Yasuda,[s] T. Ishizuka,[u] and K. Ohta[u]

[a] *University of Rochester, Rochester, NY 14627*
[b] *Louisiana State University, Baton Rouge, LA 70803*
[c] *Institute of High Energy Physics, Beijing 100039*
[d] *Virginia Polytechnic Institute and State University, Blacksburg, VA 24061*
[e] *University of South Carolina, Columbia, SC 29208*
[f] *Ohio State University, Columbus, OH 43210*
[g] *University of California, Davis, CA 95616*
[h] *KEK, National Laboratory for High Energy Physics, Ibaraki 305*
[i] *Tsukuba University, Ibaraki 305*
[j] *Konan University, Kobe 658*
[k] *University of Minnesota, Minneapolis, MN 55455*
[l] *Niigata University, Niigata 950-21*
[m] *Nihon Dental College, Niigata 951*
[n] *Rutgers University, Piscataway, NJ 08854*
[o] *University of the Philippines, Quezon City, 3004*
[p] *Saga University, Saga 840*
[q] *Korea University, Seoul 136-701*
[r] *Kyungpook National University, Taegu 702-701*
[s] *Chuo University, Tokyo 112*
[u] *Saitama University, Urawa 338*

Bibliography

[1] S.L. Wu, *Phys. Report* **107**, 59 (1984).

[2] W. Heisenberg, *Z. Phys.* **113** 61 (1939); Nature, **164** 65 (1949).

[3] E. Fermi, *Prog. Theor. Phys.* **5**, 570(1950).

[4] W.Furmanski, R. Petronzio and S. Pokoski, *Nucl. Phys.* **B155**, 253 (1979).

[5] A. Bassetto, M. Ciafaloni and G. Marchesini, *Phys. Lett.* **83B**, 207 (1978).

[6] A.Mueller, *Phys. Lett.* **104B** 161 (1981); Nucl. Phys. **B213** 85 (1983).

[7] W. Thome *et al.*, *Nucl. Phys.* **B129**, 365 (1977).

[8] Z. Koba, H.B. Nielsen, and P. Olesen, *Nucl. Phys.* **B40**, 317 (1972).

[9] R.P. Feynman, *Phys. Rev. Lett.* **23**, 1415 (1969).

[10] UA5 Collaboration, K. Alpgard *et al.*, *Phys. Lett.* **121B** 109 (1983), G.J. Alner *et al.*, *Phys. Lett.* **138B** 304 (1984); **160B** 199 (1985); **167B** 476 (1986).

[11] T.T.Chou, and C.N. Yang, *Int. J. Mod. Phys.* **A2**, 1727 (1987); Phys. Lett. **167B**, 453(1986).

[12] M. Derrick *et al.*(HRS), *Phys. Rev.* **D34** 3304 (1986); *Z. Phys.* **C35**, 323 (1987).

[13] M. Althoff *et al.*(TASSO), *Z. Phys.* **C22**, 307 (1984); W. Braunschweig *et al.*, *Z. Phys.* **C45**, 193 (1989).

[14] A. Giovannini, and L. Van Hove, *Acta Phys. Polo.* **B19**, 495 (1988), and references cited therein; *Z. Phys.* **C30**, 391 (1986).

[15] P. Carruthers, and C.C. Shih, *Int. J. Mod. Phys.* **A2**, 1447 (1987), and references cited therein.

[16] C.K. Chew, and Y.K. Lim, *Phys. Lett.* **163B**, 257 (1985).

[17] R.E. Ansorge *et al.*(UA5), *Z. Phys.* **C43**, 357 (1989).

[18] TRISTAN Project Group, *"TRISTAN Electron-Positron Colliding Beam Project"*, *KEK Report* 86-14, March 1987.

[19] AMY Collaboration, *Proposal* TRISTAN-EXP-003, November, 1984.

[20] Yiu-Hung M. Ho, *Ph.D. thesis*, Univ. of Rochester, (1990).

[21] K. Ueno, University of Rochester preprint **UR-1050** (1988).

[22] S.S. Myung, *Ph.D. thesis*, Korea Univeristy, (1988).

[23] F. Kajino, A. Abashian, and K. Gotow, *Nucl. Instrum. Meth.* **A245**, 507 (1986).

[24] Y. Doi *et al.*, *Nucl. Instrum. Meth.* **A274**, 95(1989)

[25] S. Igarashi, *Ph.D. thesis*, Tokyo Institute of Technology, (1988).

[26] S.K. Kim, *Ph.D. thesis*, Korea University, (1988).

[27] T. Mori, *Ph.D. thesis*, Univ. of Rochester, (1988).

[28] T. Sjöstrand, *Com. Phys. Comm.* **39**, 347 (1986).

[29] F. Gutbrod, G. Kramer, G Schierholz, *Z. Phys.* **C21**, 235 (1984)

[30] B Anderssen, G. Gustatsson, G. Ingelman, T. Sjöstrand, *Phys. Rep.* **97**,33 (1983)

[31] T. Sjöstrand, M. Bengtsson, *Com. Phys. Comm.* **43**, 367 (1987).

[32] W. Bartel *etal.* (JADE), *Z. Phys.* **C25**, 231 (1984); **C33**, 23 (1986).

[33] S. Bethke, *Heidelberg Habilitation Thesis* LBL 50-208 (1987); W. Braunschweig *etal.* (TASSO), *DESY* 88-046 (1988).

[34] I. Park, (AMY), *KEK* 88-45 (1988), *Ph.D. thesis*, Rutgers University, (1989).

[35] The parameters used in the Lund 6.3 (Parton-Shower) model are: $\Lambda_{LLA} = 0.40$ GeV; cascade virtuality cutoff $Q_0 = 1.0$ GeV; fragmentation parameter $a = 0.50$; fragmentation parameter $b = 0.9$ GeV^{-2}; gaussian P_T parameter $\sigma_q = 0.35$ GeV/c.

[36] Y.K. Li *et al.* (AMY), *Phys. Rev.* **D41**, 2675 (1990).

[37] W.R. Nelson *et al.*, *"The EGS4 code system"*, SLAC-Report-265 (1985).

[38] A. Grant, *Nucl. Instrum. Meth.* **131**, 167 (1975).

[39] T. Mori, *Ph.D. thesis*, Univ. of Rochester, Appendix A (1988).

[40] T. Mori, *Ph.D. thesis*, Univ. of Rochester, Appendix B (1988).

[41] D. G. Cassel and M. Ogg, *"DUET - a Track-Finding Program for Cylindrical Geometries", CLEO internal Report (1983).*

[42] D. G. Cassel and H. Kowalski, *Nucl. Instrum. Meth.* **185**, 235 (1981).

[43] J.D. Bjorken and S.D. Drell *Relativistic Quantum Mechanics*. McGraw-Hill, New York (1964).

[44] C. Bacci *et al.*(ADONE), Phys. Lett. **86B**, 234 (1979); C. Berger *et al.*(PLUTO), Phys. Lett. **95B**, 313 (1980); B.Niczyporuk *et al.*(LENA), Z. Phys. **C9**, 1 (1981); J.L Siegrist *et al.*(MARKI), Phys. Rev. **D26**, 969 (1982); W. Bartel *et al.*(JADE), Z. Phys. **C20**, 187 (1983); M. Yamauchi (TOPAZ) in: *XXIV International Conference on High Energy Physics*, edited by R. Kotthaus and J.H. Kuhn (Springer-Verlag,1988).

[45] D. Decamp *et al.*(ALEPH), CERN preprint EP/89-139; G.S. Abrams *et al.*(MARKII), SLAC preprint PUB-5092.

[46] H. Satz, in *Current Induced Reactions*, edited by J.G.Körner, G. Kramer, and D. Schildknecht, (Lecture Notes in Physics), P.49, Vol.56 (Springer - Verlag, 1975).

[47] The design of the wire holding bushing was adapted from the one developed by T. Kondo for the VENUS experiment at TRISTAN.